Search for Dark Matter in Association with a Boosted Heavy Scalar in Semileptonic Signatures with the ATLAS Experiment

Ludwig-Maximilians-Universität München
Faculty of Physics

David Koch

April 2020

Suche nach dunkler Materie in Assoziation mit einem geboosteten schweren skalaren Teilchen im semileptonischen Kanal mit dem ATLAS Experiment

Ludwig-Maximilians-Universität München
Fakultät für Physik

David Koch

April 2020

Supervisor: Prof. Dorothee Schaile

Abstract

Many searches for new phenomena in the field of experimental high energy physics look for dark matter. This analysis presents a search for dark matter that is produced via a new heavy mediator Z' and in association with a boosted dark Higgs boson s that decays into two W-bosons. The parameters of this model are chosen in a way that it is able to reproduce the relic dark matter abundance, a main motivation for this model. The signature where the W-bosons decay semileptonically, resulting in the presence of one charged lepton, a large-R jet and missing transverse energy, is studied.

Monte Carlo simulations of pp-collisions at the LHC with a center of mass energy of $\sqrt{s} = 13\,\text{TeV}$ at the ATLAS detector are used. The use of track-assisted reclustered (TAR) jets with radius parameters $R = 0.6$, $R = 0.8$, $R = 1.0$ and standard anti-k_t jets with $R = 1.0$ (large-R jets) to reconstruct the hadronically decaying boosted W-boson is studied. Then, an optimization of selection criteria to define the signal region is presented, cross-checked and verified. The expected significance and exclusion limit is calculated. The expected exclusion limit is further improved by splitting up the signal region into multiple subregions, resulting in an expected exclusion of the masses $m_{Z'} < 2500\,\text{GeV}$ and $m_s < 300\,\text{GeV}$ at 95 % confidence level.

Zusammenfassung

Viele Suchen nach neuen Phänomenen in der Hochenergiephysik suchen nach dunkler Materie. Diese Analyse zeigt eine Suche nach dunker Materie, die über ein neues schweres Mediator-Teilchen Z' und in Assoziation mit einem dunklen Higgs-Boson s, das in zwei W-Bosonen zerfällt, produziert wird. Die Paramter des Modells sind so gewählt, dass es die Dichte der dunklen Materie zum Zeitpunkt des thermischen Einfrierens des Universums reproduzieren kann, eine der Hauptmotivationen dieses Modells. Die Signatur, bei der die W-Bosonen semileptonisch zerfallen, was zu einem geladenen Lepton, einem großen Jet und fehlender transversaler Energie führt, wird untersucht.

Monte Carlo Simulationen von pp-Kollisionen am ATLAS Detektor am LHC bei einer Schwerpunktsenergie von $\sqrt{s} = 13\,\text{TeV}$ werden dazu verwendet. Die Verwendung von spur-gestützten reclustered (TAR) Jets mit den Radius-Parametern $R = 0.6$, $R = 0.8$, $R = 1.0$ sowie von Standard-anti-k_t Jets mit $R = 1.0$ für die Rekonstruktion des hadronisch zerfallenden geboosteten W-bosons wird untersucht. Weiterhin wird eine Optimierung von Selektionskriterien für die Definition einer Signalregion gezeigt, überprüft und verifiziert. Die erwartete Signifikanz und Ausschlussgrenze wird berechnet. Die erwartete Ausschlussgrenze wird durch das Aufteilen der Signalregion in mehrere Subregionen weiter verbessert, so dass das schlussendlich erwartete Limit die Massen $m_{Z'} < 2500\,\text{GeV}$ und $m_s < 300\,\text{GeV}$ bei einem Konfidenzniveau von 95 % ausschließt.

Contents

1 Introduction

All fields of physics pose certain questions to nature and so does the field of particle physics. Particle physics however stands out in a way, as it asks questions that touch the very core of physics. To understand why an object appears in a certain color, one needs to understand the material it is made of. To truly understand the material, one needs to understand the atoms it is made of and how they are arranged. To truly understand the atom, one must understand that it is made of electrons and a nucleus and how they interact. To put it in the words of Carl Sagan: "If you wish to make an apple pie from scratch, you must first invent the universe". The questions posed in particle physics are among the most fundamental ones a natural science can ask, touching the "invention of the universe": What are the fundamental building blocks of matter? How do elementary particles interact with other elementary particles? What kinds of elementary particles are there?

Answering these questions requires two tactics: Constructing theoretical frameworks that are consistent with previous observations and are able to make testable predictions, and perform experiments that allow us to decide which of the proposed theories are more correct than others, and rule those others out. The standard model of particle physics (SM) is currently the best theory we have, being able to accurately describe a large variety of phenomena in particle physics. However, there are still many open questions. The SM is not able to explain for example gravity or dark matter. Therefore many theories, including supersymmetric theories and simplified models, aim to address the various problems the SM has. The Large Hadron Collider (LHC), together with the four detectors ATLAS, CMS, LHCb and ALICE at CERN is currently the largest experiment in the world to search for new physics and probe the SM at high precision.

This analysis presents a search for dark matter at the ATLAS detector as proposed by a simplified extension to the SM introducing a dark matter particle χ, a heavy mediator Z' between the dark matter and SM particles and an additional dark Higgs boson s. It focuses on the case of a boosted heavy dark Higgs boson that decays semileptonically via two W-bosons. It is structured as follows: First, an introduction to the theory of the SM is given, together with an overview of the motivation and theoretical background of the dark matter model considered. Then, the experimental setup at the LHC and ATLAS specifically is shown and explained. After discussing the generation of Monte Carlo (MC) simulated data, the reconstruction of the data into physical objects is presented and defined. Finally, the analysis of the MC generated data is shown. First, the signature of the considered signal model is explained. Then, a study is presented which jet reconstruction technique works best in order to reconstruct the hadronically decaying W-boson in this analysis. Then, the signal region is optimized, followed by a statistical analysis of the MC data.

2 Theoretical background

2.1 The standard model of particle physics

The standard model of particle physics (SM) is the theoretical framework for describing three of the four fundamental forces of nature: the electromagnetic force, the weak force and the strong force. Gravity is not included in the SM as it is too weak to have a measurable effect at collider experiments at the energy scale current particle colliders can achieve.

Being the most fundamental theory of nature that we have at hand at present the SM has been widely successful, for example by predicting the existence of particles before their discovery like the charm quark [1] or the Higgs boson [2, 3]. Since the Higgs boson was discovered in 2012 [4, 5], all particles of the SM have been observed.

The particle content as well as the mathematical framework for the SM will be discussed in the following sections.

2.1.1 Particle content

In general, one can divide all particles into fermions and bosons, where fermions are particles with half-integer spin and bosons particles with integer spin. The fermions of the SM are listed in tab. 2.1. They are further subdivided into *leptons* and *quarks*. Every fermion

name	**symbol**	**el. charge**	**weak isospin $I_W^{(3)}$**	**color**
		leptons		
electron	e^-	-1	$-\frac{1}{2}$	-
electron-neutrino	ν_e	0	$+\frac{1}{2}$	-
muon	μ^-	-1	$-\frac{1}{2}$	-
muon-neutrino	ν_μ	0	$+\frac{1}{2}$	-
tau	τ^-	-1	$-\frac{1}{2}$	-
tau-neutrino	ν_τ	0	$+\frac{1}{2}$	-
		quarks		
up	u	$+2/3$	$+\frac{1}{2}$	r,g,b
down	d	$-1/3$	$-\frac{1}{2}$	r,g,b
charm	c	$+2/3$	$+\frac{1}{2}$	r,g,b
strange	s	$-1/3$	$-\frac{1}{2}$	r,g,b
top	t	$+2/3$	$+\frac{1}{2}$	r,g,b
bottom	b	$-1/3$	$-\frac{1}{2}$	r,g,b

Table 2.1: The fermions of the SM. Electric charge is given in units of e. The third component of the weak isospin $I_W^{(3)}$ is listed here only for left-handed particles, as it is 0 for all right-handed particles.

in the SM has a corresponding *antiparticle* that has exactly the same mass but opposite quantum numbers. These are usually denoted by adding an overline to the symbol for the particle.

The bosons of the SM play the role of exchanging forces between other particles. Which boson carries which force is listed in tab. 2.2. With the exception of the $W^{\pm}$ bosons, none carry electric charge.

name	**symbol**	**associated force**	**spin**
photon	γ	electromagnetic force	1
Z boson	Z	weak force (neutral currents)	1
W boson	$W^{\pm}$	weak force (charged currents)	1
gluon	g	strong force	1
Higgs boson	H	(Higgs field)	0

Table 2.2: Bosons of the SM. The role of the Higgs boson differs from the bosons that carry a fundamental force, see sec. 2.1.2.

2.1.2 Quantum field theories

The theoretical framework for the SM is that of a *quantum field theory* (QFT). A QFT both respects the aspects of quantum mechanics, which is crucial when dealing with elementary particles, as well as special relativity, which will play a role when dealing with high energies. This section aims to give an overview to QFT in general as well as the QFTs that are built into the SM.

Lagrange formalism in quantum field theories

In classical mechanics, the notion of a "particle" is that of a point-like, massive object with precise position $\vec{x}$ and velocity $\dot{\vec{x}}$. A system consisting of N such particles can for example be described by the Lagrange formalism. The Lagrange formalism introduces the *Lagrange function* $L(q_i, \dot{q}_i)$, $i = 1 \dots N$ which depends on the generalized coordinates $q_i(t)$ and $\dot{q}_i(t)$ of the particles where $\dot{q}_i$ denotes the time derivative of q_i[1]. The actual dynamics of such a system are then dictated by the *principle of stationary action*[2], which states that the particle or particles take a path where the action is stationary [7]. The action is defined as the time integral of the Lagrange function:

$$\mathcal{S} = \int L\big(q_i(t),\, \dot{q}_i(t)\big)\, \mathrm{d}t. \tag{2.1}$$

Mathematically, the principle of stationary action can be expressed as

$$\delta\mathcal{S} = 0. \tag{2.2}$$

From eq. (2.2) and the assumption that variations of q_i vanish at the borders of integration, the *Euler-Lagrange-Equations* follow:

$$\frac{\partial L}{\partial q_i} - \frac{\mathrm{d}}{\mathrm{d}t}\left(\frac{\partial L}{\partial \dot{q}_i}\right) = 0. \tag{2.3}$$

This set of equations of motion (one for each i) allows us to determine how the physical system develops over time by solving the differential equations for $q_i(t)$.

In a quantum field theory however, particles are not described by discrete points, but by fields $\phi(\vec{x}, t)$ that are defined for every point $x = (t, \vec{x})$ in spacetime. It is helpful to think

[1] In principle, the Lagrange function can also depend explicitly on the time, however this spoils energy conservation and thus will never be the case for closed systems [6].

[2] also known as *Hamilton's principle*

of making a transition $q \to \phi$ and changing the discrete index i to a continuous "index" $(\vec{x}, t)$, ultimately leading to $q_i(t) \to \phi(\vec{x}, t)$. This is of course only heuristics, but it helps to see the analogy to classical mechanics. The Euler-Lagrange-Equations for a relativistic field theory are then:

$$\frac{\partial \mathcal{L}}{\partial \phi} - \partial_\mu \left(\frac{\partial \mathcal{L}}{\partial(\partial_\mu \phi)} \right) = 0 \tag{2.4}$$

where $\mathcal{L}$ is the Lagrange-density or *Lagrangian*, defined via $L = \int \mathcal{L}\, \mathrm{d}^3x$. Instead of depending on the generalized coordinates and their time derivatives, the Lagrangian now depends on the fields ϕ and their derivatives $\partial_\mu \phi$. The second term in eq. (2.4) uses Einstein-summation. This convention implies that any summation $\sum_{\mu,\nu} x^\mu x^\nu \eta_{\mu\nu}$ can be abbreviated as $x^\mu x_\mu$ where $\eta_{\mu\nu}$ is the Minkowski metric, implementing accordance with special relativity.

An example is the Lagrangian for a Dirac field describing a free spin-$\frac{1}{2}$ particle:

$$\mathcal{L} = \overline{\psi} i \gamma^\mu \partial_\mu \psi - m \overline{\psi} \psi. \tag{2.5}$$

Here, $\psi(x)$ and $\overline{\psi}(x)$ are the Dirac field and its conjugate, γ^μ are 4×4 matrices satisfying the anticommutator relation $\{\gamma^\mu, \gamma^\nu\} \coloneqq \gamma^\mu \gamma^\nu + \gamma^\nu \gamma^\mu = 2\eta^{\mu\nu}$ and m is a positive real number, associated with the mass of the particle. Applying eq. (2.4) to this Lagrangian leads to the two[3] Dirac equations

$$i \gamma^\mu \partial_\mu \psi - m \psi = 0 \tag{2.6}$$

$$i \partial_\mu \overline{\psi} \gamma^\mu + m \overline{\psi} = 0. \tag{2.7}$$

The solutions to these equations correspond to freely moving particles and antiparticles with half-integer spin, for example electrons or positrons [8].

Quantum Electrodynamics

Quantum electrodynamics (QED) is the theory to describe interactions between electrically charged elementary particles. For a start we look at the Dirac Lagrangian (2.5) for a free spin-$\frac{1}{2}$ particle. It is invariant under the global phase transformation

$$\psi \to \psi' = e^{-iq\chi} \psi, \quad q\chi \in \mathbb{R} \tag{2.8}$$

and the equivalent transformation for the conjugate field $\overline{\psi}$. It is not invariant under *local* phase transformations $\psi \to e^{-iq\chi(x)} \psi$, where χ is dependent on the spacetime coordinate x. It can however be made invariant under such a local phase transformation by introducing a new vector field A_μ that transforms like

$$A_\mu \to A'_\mu = A_\mu + \partial_\mu \chi(x) \tag{2.9}$$

and adding the term $-\overline{\psi} \gamma^\mu q A_\mu \psi$ to the Lagrangian. Invariance under such a transformation is called $U(1)$ *gauge symmetry*. It is convenient to define the *covariant derivative* $D_\mu \coloneqq \partial_\mu + iqA_\mu$ so that the new Lagrangian can be written as

$$\mathcal{L} = \overline{\psi} i \gamma^\mu D_\mu \psi - m \overline{\psi} \psi. \tag{2.10}$$

The vector potential A_μ describes the photon field that interacts with particles and antiparticles with a coupling strength q corresponding to the electric charge of the particle. To

[3] There are two equations of motion because the Lagrangian depends on two independent fields ψ and $\overline{\psi}$, however one usually only refers to eq. (2.6) as *the* Dirac equation.

allow for free photons there needs to be an additional term that produces the free Maxwell equations when applied to the Euler-Lagrange-Equations. This term is given by $\frac{1}{4}F_{\mu\nu}F^{\mu\nu}$ where $F_{\mu\nu} \coloneqq \partial_\mu A_\nu - \partial_\nu A_\mu$. The full Lagrangian for QED is then:

$$\mathcal{L}_{\text{QED}} = \overline{\psi} i\gamma^\mu D_\mu \psi - m\overline{\psi}\psi - \frac{1}{4}F_{\mu\nu}F^{\mu\nu}. \tag{2.11}$$

The solution to the resulting equations of motion can only be calculated perturbatively. There is however a nice way of representing the calculations in a graphical way with the help of *Feynman graphs*. In such a graph, lines represent particles and vertices of lines

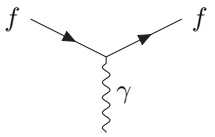

(a) Fundamental vertex of QED

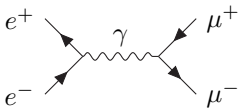

(b) Electron and positron annihilating to a muon pair

Figure 2.1: Examples of Feynman graphs of QED. f represents any charged fermion, γ the photon and $e^\pm$ and $\mu^\pm$ (anti-) electrons and (anti-) muons.

represent interactions between particles. Fig. 2.1a shows the only possible vertex of QED. Straight lines with an arrow to the right represent fermions while straight lines with an arrow to the left represent the corresponding antiparticle. Curvy lines represent photons. Fig. 2.1b shows the lowest order Feynman graph for an electron and a positron annihilating into a pair of muons [8]. The diagrams are to be read from left to right in time, so that lines at the left side of the diagram denote incoming particles and lines on the right side denote outgoing particles.

Electroweak theory

Much like electromagnetism unites the theory of electricity with the theory of magnetism, the electroweak theory—as the name suggests—is a theory of both electromagnetic and weak interactions, which for example drive the β-decay of the neutron or the decay of the muon (see fig. 2.2b). So it makes sense to say that the SM actually describes two forces instead of three, as the electromagnetic and weak force are united under one electroweak theory, also called Glashow-Weinberg-Salam theory (GWS-theory) [9].

The theoretical discription of charged weak interactions is obtained in a similar way as in QED. Requiring invariance under a local $SU(2)_L$ transformation[4]

$$\varphi(x) \to \varphi'(x) = \exp\left(\frac{ig}{2}\,\vec{\alpha}(x)\cdot\vec{\sigma}\right)\varphi(x) \tag{2.12}$$

where g is the coupling constant, the components of $\vec{\sigma}$ are the Pauli matrices[5] and $\vec{\alpha}$ are three arbitrary real functions of x, gives rise to three gauge fields W_μ^i that are associated with three gauge bosons $W^{(i)}$ with $i = 1, 2, 3$. The field φ has two components, sorting all weakly interacting particles into *weak isospin doublets* for lefthanded particles of total weak isospin $I_W = \frac{1}{2}$

$$\begin{pmatrix}\nu_e\\ e^-\end{pmatrix}_L, \quad \begin{pmatrix}\nu_\mu\\ \mu^-\end{pmatrix}_L, \quad \begin{pmatrix}\nu_\tau\\ \tau^-\end{pmatrix}_L, \quad \begin{pmatrix}u\\ d'\end{pmatrix}_L, \quad \begin{pmatrix}c\\ s'\end{pmatrix}_L, \quad \begin{pmatrix}t\\ b'\end{pmatrix}_L$$

[4] The subscript L stands for "left" and indicates that this transformation only affects left-handed particles and right-handed antiparticles.

[5] In fact they can be any set of three matrices that form a basis for the $SU(2)$ group.

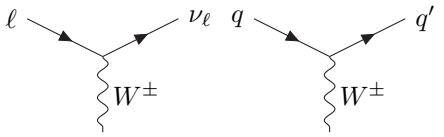

(a) Vertices for a W boson interacting with leptons and quarks. ℓ denotes any charged lepton and ν_ℓ the corresponding neutrino. q and q' can be any up-type and down-type quarks, respectively.

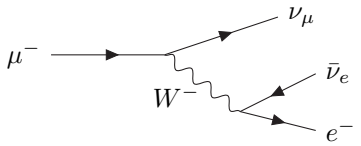

(b) Muon decaying into an electron and neutrinos via a W^- boson.

Figure 2.2: Examples of Feynman graphs showing charged weak interactions.

and weak isospin singlets with $I_W = 0$ that do not couple to any of the gauge bosons $W^{(i)}$. The quarks d, s and b are dashed here to indicate that the weak isospin doublets contain the weak eigenstates of the quarks, which differ from their mass eigenstates (which are denoted without a dash). Also, the physical $W^\pm$ bosons are not the gauge bosons themselves but rather linear combinations thereof:

$$W_\mu^\pm = \frac{1}{\sqrt{2}} \left(W_\mu^{(1)} \mp W_\mu^{(2)} \right). \tag{2.13}$$

The fundamental vertices for an interaction between a W boson and a fermion are shown in fig. 2.2a [8, 9].

The unification with QED follows from requiring invariance under local $U(1)$ transformations again. This gives rise to a new gauge field B_μ. Notice that it is not the same as A_μ in QED—rather, A_μ is a linear combination of the gauge fields B_μ and $W_\mu^{(3)}$. There also must be a second neutral gauge boson, called Z, behaving in much the same way as the photon but coupled to the hypercharge $Y = 2(Q - I_W^{(3)})$ with coupling constant g'. These gauge bosons can be expressed in terms of the gauge fields

$$\begin{pmatrix} A_\mu \\ Z_\mu \end{pmatrix} = \begin{pmatrix} \cos\theta_W & \sin\theta_W \\ -\sin\theta_W & \cos\theta_W \end{pmatrix} \cdot \begin{pmatrix} B_\mu \\ W_\mu^{(3)} \end{pmatrix} \tag{2.14}$$

where θ_W is called the *Weinberg angle* or *weak mixing angle*. It is related to the unit of electric charge via the relation $e = g \sin\theta_W = g' \cos\theta_W$ [10].

The Higgs mechanism

The GWS-theory still has some problems. First, it violates quantum mechanical unitarity, meaning that the cross section of e.g. the process $e^+e^- \to W^+W^-$ grows without bound with increasing center of mass energy [9]. Second, the gauge bosons Z, γ and $W^\pm$ are massless in the GWS-theory. They are so for consistency reasons—it is impossible to introduce mass terms to the electroweak Lagrangian without breaking its gauge invariance. This however conflicts with what we observe in nature as the Z and $W^\pm$ are in fact quite heavy[6] [11, 12]:

$$m_Z = 91.1875 \pm 0.0021\,\text{GeV} \tag{2.15}$$

$$m_W = 80.376 \pm 0.033\,\text{GeV}. \tag{2.16}$$

The Higgs mechanism provides a way to explain where the masses of the $W^\pm$ and Z come from and solve the unitarity problem. The general idea is to construct a Lagrangian that

[6] Throughout this thesis $\hbar \equiv c \equiv 1$ and masses are given in units of eV.

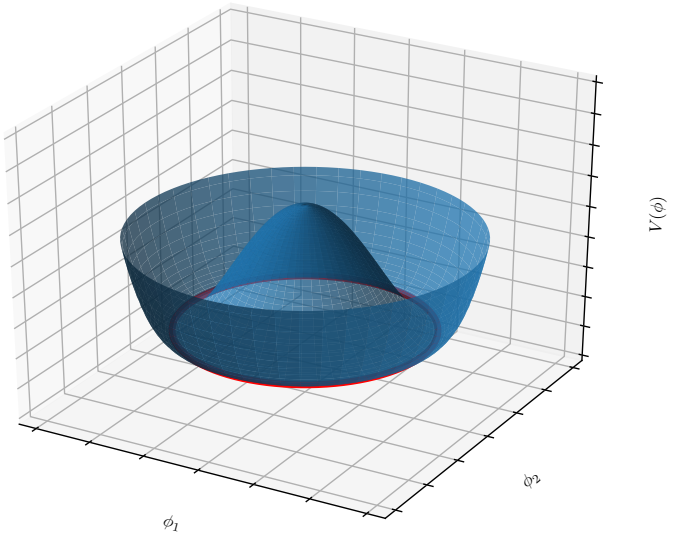

Figure 2.3: Visual representation of the potential V(ϕ) (2.18) with $\lambda^2 > 0$ and $\mu^2 > 0$. The x and y axis show the real and imaginary part of ϕ. The possible ground states where the symmetry is broken are marked with a red line.

is still gauge invariant, but has a ground state that breaks this symmetry. This is called *spontaneous symmetry breaking*.

Consider for example this Lagrangian that is invariant under global $SU(2)$ and $U(1)$ transformations:

$$\mathcal{L} = \frac{1}{2}(\partial_\mu \phi)^\dagger (\partial^\mu \phi) - V(\phi) \tag{2.17}$$

$$V(\phi) = -\frac{1}{2}\mu^2 \phi^\dagger \phi + \frac{1}{4}\lambda^2 \left(\phi^\dagger \phi\right)^2 \tag{2.18}$$

where $\phi = \phi_1 + i\phi_2$ is a complex scalar field, $\lambda^2 > 0$ and $\mu^2 > 0$. The corresponding ground states lie on a circle with radius $\frac{\mu}{\lambda}$ (see fig. 2.3). If we choose the ground state to be $\phi_0 = \frac{\mu}{\lambda}$ and rewrite the Lagrangian in terms of two new fields $\eta := \phi_1 - \frac{\mu}{\lambda}$ and $\xi := \phi_2$ it becomes apparent that the field η has a mass term with mass $\sqrt{2}\mu$ and the field ξ is massless. The Lagrangian in terms of η and ξ is not invariant anymore, the symmetry is "lost" by choosing a particular ground state over the symmetric set of all possible ground states, thus the term spontaneous symmetry breaking [8, 10].

If we now take the Lagrangian from eq. (2.17), require local $SU(2)_L \otimes U(1)_Y$ gauge invariance (see section 2.1.2 on electroweak theory) and repeat the procedure of spontaneous symmetry breaking, the fields $W_\mu^\pm$ and Z_μ acquire a mass related via the equation

$$m_W = m_Z \cos\theta_W. \tag{2.19}$$

The $U(1)$ subgroup of QED remains unbroken, so the photon is still massless. Analogous to ξ in the discussion above, three massless bosons should appear. Their degrees of freedom however went into the longitudinal polarizations the $W^\pm$ and Z can have now that they are massive so no additional massless bosons are present[7] [13]. What remains is a new massive scalar particle (η in the discussion above), called the Higgs boson [10]. It couples

[7] This is achieved by choosing a certain gauge, called the *unitarity gauge* which transforms the additional three massless bosons away. In the literature, it is often said that the $W^\pm$ and Z "eat" these bosons [13].

to every particle that has mass—that is every particle of the SM except neutrinos[8], gluons and photons—and with a strength roughly proportional to their mass.

This mechanism is a clever way of allowing gauge bosons to have mass, while guaranteeing gauge invariance of the Lagrangian and additionally predicting the existence of the Higgs boson without which the SM would have been an inconsistent theory.

Quantum Chromodynamics

Quantum chromodynamics (QCD) is the theory of strong interactions. It applies only to quarks and antiquarks since they are the only fermions that carry color charge (color and anticolor), the charge of the gluon field. The color of a quark can take any value of $\{r, g, b\}$ (red, green, blue) and the opposite color charges for antiquarks are $\{\bar{r}, \bar{g}, \bar{b}\}$. The term color is chosen for this kind of charge because the addition of color charges matches our intuition of the addition of colors: a color and its anticolor combined result in a colorless state and a state combining all three (anti-)colors to an equal amount is colorless as well. The gluons, the gauge bosons of QCD and force carriers of the strong force, each have a color and an anticolor. Because there are nine ways to combine a color and an anticolor, there are in principle nine possible states for gluons. However, just like QED has $U(1)$ as its underlying symmetry and GWS-theory has $SU(2)_L \otimes U(1)_Y$ symmetry, QCD is invariant under transformations of the $SU(3)$ symmetry group and it turns out that under $SU(3)$, these nine gluon states come as an octet with eight states plus one singlet state. This singlet state would allow for a long-range strong force which is not observed in nature. It is therefore not considered and the number of gluons in the SM is eight [8].

QCD has a peculiar quality: because the gluons carry color charge themselves, a gluon can directly interact with another gluon (unlike, for example, photons). This feature makes the coupling constant α_s highly dependent on the energy scale in an interesting way—α_s gets smaller with larger energies and smaller distances. This phenomenon is known as *asymptotic freedom*. It means that at lower energy, like for example in a bound state like the proton or neutron, α_s gets that large that a perturbative treatment of QCD becomes impossible, while it gets increasingly more accurate at higher energies.

Another feature of strong interactions with interesting implications is the *color confinement hypothesis*. It is a hypothesis because it does not follow necessarily from the theory—it is rather an observational fact. It says that any free particle must be colorless. This means that we will never be able to directly measure a single gluon or quark. As a consequence, when quarks or gluons are produced in a hard scattering event, they cannot simply "fly away" independently. They do so only for the first $10^{-15}\,m$ during which they experience their asymptotic freedom until the strong force becomes that large that new quark-antiquark pairs and gluons are produced. This process is called *hadronisation* and is repeated as long as there is enough energy left to produce new quarks. Eventually they form colorless bound states, so called *hadrons*, that either decay or are measured directly in a detector. The cascades of hadrons that emerge from a quark or gluon in a scattering process are called *jets* [8, 15, 16].

For further discussion of the term jets and its definition, see sec. 5.1.4.

2.1.3 Limitations of the SM

Although the SM is able to describe nature to an impressive accuracy, there are still open questions. Apart from the fact that the SM is not able to describe gravity, it also does not

[8] In fact, neutrinos do have a mass larger than zero [14] but it is so miniscule that neutrinos are assumed to be massless in this analysis.

include dark matter, which is estimated to make up about 25 % of the energy density of our universe [17]. The matter known to us that makes up everything from our everyday life to the visible night sky only contributes 5 % of the total energy density of our universe [17, 18]. Evidence for the existence of dark matter comes e.g. from the observation of spiral galaxy arms whose motion is way too fast to be explained by the pull of visible matter only and from the analysis of the power spectrum of the cosmic microwave background [19–22].

The most obvious way to explain this phenomenon is to postulate that there exists a kind of matter that consists of massive elementary dark matter particles that interact either only gravitationally or gravitationally and weakly. They cannot interact with photons or gluons, otherwise they would have been observed already [23]. In fact, neutrinos have these features. They are however too light to make up for large amounts of cold dark matter[9] [24]. This means that the astrophysical observations of dark matter cannot be explained by the SM and we need to extend the SM and find a more fundamental theory of nature.

There are already several very promising models that could explain dark matter, many of which fall under the category of *supersymmetric theories* (SUSY). Another interesting approach is to not specify a completely mature theory, but rather extending the SM in a minimal way by introducing only a dark matter candidate and a new mediator between SM particles and dark matter [25].

The model considered in this thesis is such a simplified model. It has the advantage of being able to reproduce the relic density of dark matter[10] without being too constrained by previous searches [26].

2.2 A simplified model for Dark Matter

The general idea of the simplified model considered in this thesis is to only introduce three new particles: a Majorana[11] dark matter particle χ, a weak mediator Z' and a dark Higgs field S for the generation of masses in the dark sector with an associated dark Higgs boson s. "Simplified" means here that certain couplings are ignored (see discussion below) and no additional particles are introduced.

According to ref. [26], the Lagrangian of this model is given by

$$\mathcal{L}_\chi = -\frac{1}{2} g_\chi Z'^\mu \bar{\chi} \gamma^5 \gamma_\mu \chi - g_\chi \frac{m_\chi}{m_{Z'}} s \chi \bar{\chi} + 2 g_\chi Z'^\mu Z'_\mu (g_\chi s^2 + m_{Z'} s) \tag{2.20}$$

with the free parameters g_χ, m_χ, $m_{Z'}$ and m_s. g_χ is the coupling strength between the Z' and the χ, m_χ is the mass of the dark matter candidate, $m_{Z'}$ is the mass of the Z' and m_s is the mass of the dark Higgs boson s. The mediator Z' can be seen as a heavy partner of the SM Z-boson as it is the gauge boson of a new symmetry $U(1)$. By spontaneously breaking this symmetry through a new Higgs field S, the Z' acquires its mass and a new Higgs boson s, called *dark Higgs*, emerges.

The first term in eq. (2.20) is responsible for an axial coupling between the Z' and the dark matter particle χ (see fig. 2.4a). Axial coupling means that this interaction violates parity. A parity conserving interaction between χ and Z' would in principle be possible if χ was not a Majorana particle, but this would introduce another free parameter and is therefore not considered here for simplicity. The second term couples the dark Higgs to the dark matter (see fig. 2.4b) and the last term of $\mathcal{L}_\chi$ results in two vertices (see fig. 2.4c) coupling the Z' to the dark Higgs—this way, all three particles from the dark sector are connected.

[9] "Cold" dark matter means dark matter that is not moving at high speeds.

[10] That is the density of dark matter in the universe at the time of thermal freeze-out.

[11] A Majorana particle is a fermion that is its own antiparticle.

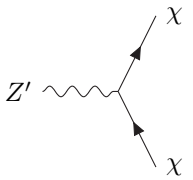

(a) Axial coupling of the Z' to dark matter.

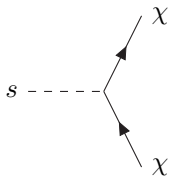

(b) Coupling of the dark Higgs s to dark matter.

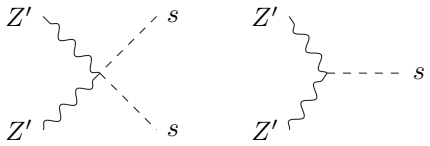

(c) Couplings of the Z' to the dark Higgs s.

Figure 2.4: Vertices that follow from the Lagrangian for the dark sector in eq. (2.20).

To connect the dark sector to the SM, the Z' also couples to quarks with the coupling strength g_q. Possible couplings to leptons are assumed to be negligible for simplicity. Furthermore, the dark Higgs mixes with the SM Higgs and can therefore decay directly into SM particles [26].

2.2.1 Signal Model

To probe this theory, specific values of the free parameters need to be set to construct a signal model. The most appealing way to choose the masses of the three new particles is such that $m_{Z'} \gg m_Z$ because invisible decays of the Z are already strongly constrained by results by LEP [12]. The dark Higgs should be the lightest particle, so that the relic abundance of dark matter in the universe is mainly set by the annihilation process $\chi\chi \to ss$ which loosens the constraints on parameter space set by previous measurements [26, 27]. If the dark Higgs mixes with the SM Higgs like proposed in this model, the only possible way for the s to decay further is then into SM particles. Fig. 2.5 shows the leading order Feynman diagrams how dark matter in association with this dark Higgs boson could be produced at LHC and then decay further. In this analysis, the case is considered where $m_s > 2m_W$ so that the branching fraction of $s \to WW$ dominates the decay of the dark Higgs. Smaller dark Higgs masses have already been studied by ref. [28]. The decay $s \to ZZ$ is also possible but not considered in this analysis since it cannot have a single lepton in its final state (given that all leptons are reconstructed correctly). One of the W bosons then decays leptonically, the other one hadronically. The case of both Ws decaying hadronically is already covered by [29].

The coupling constants are set to

- $g_q = 0.25$
- $g_\chi = 1$

in accordance with previous searches [26, 30].

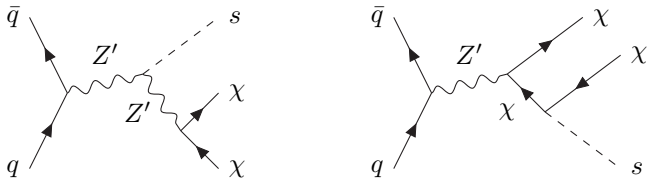

(a) Production of a dark Higgs s in association with dark matter.

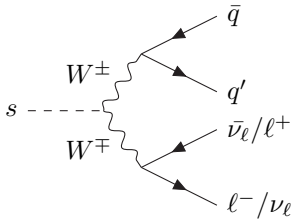

(b) Decay of the dark Higgs into two W bosons that decay semileptonically.

Figure 2.5: Production and decay of the dark Higgs boson s in this analysis. χ denotes the dark matter candidate and Z' the mediator. In this analysis, only the cases where ℓ is either an electron or a muon is considered.

3 Experimental setup

3.1 The Large Hadron Collider

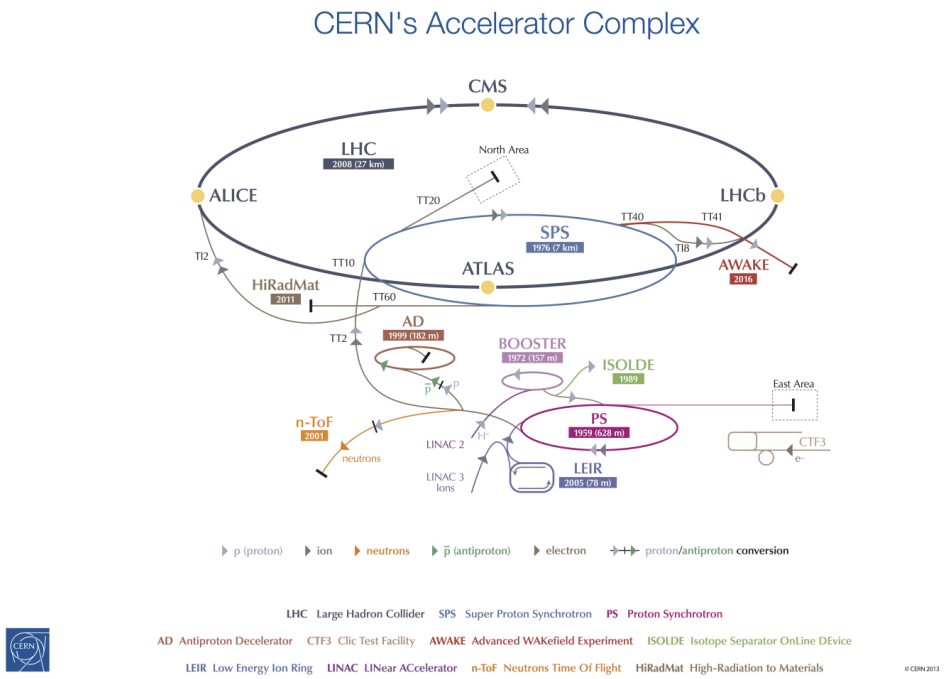

Figure 3.1: The CERN accelerator complex [31].

The Large Hadron Collider (LHC) [32] at CERN in Geneva, Switzerland, is currently the largest particle accelerator in the world. It is designed to accelerate and collide hadrons to an hitherto unmatched center of mass energy of up to $\sqrt{s} = 14\,\text{TeV}$ in a 26.7 km long tunnel $45 - 150\,\text{m}$ under the ground (see fig. 3.1). For protons, the particles with which the LHC is filled most of the times, this center of mass energy corresponds to a speed of 99.999999 % of the speed of light [33]. To date, the LHC runs at a center of mass energy of $\sqrt{s} = 13\,\text{TeV}$.

The protons are packed in *bunches* with a size of $2.5\,\mu\text{m}$, containing 1.15×10^{11} protons each [34]. The bunches cross each other at eight locations in the LHC. Four collision points are equipped with particle detectors dedicated for specific physics goals (see fig. 3.1). ALICE [35] is a detector built to record collisions of Pb-ions to study quark-gluon-plasma. LHCb [36] is an asymmetric particle detector specialized to study physics of b-hadrons to investigate CP-violating phenomena. ATLAS and CMS [37, 38] are multi-purpose experiments using different strategies and technologies to reliably cross-check each other. The ATLAS detector is presented in the following section.

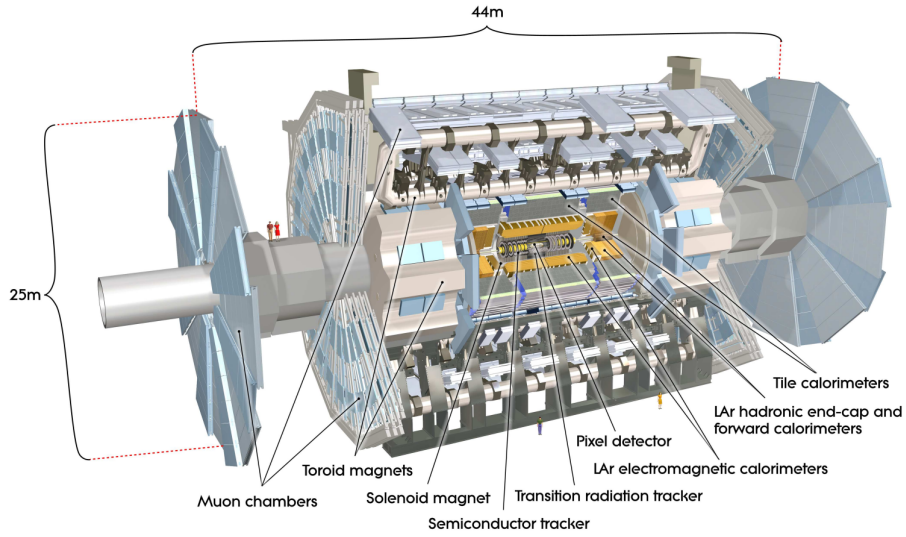

Figure 3.2: Schematic view of the ATLAS detector [37].

3.2 The ATLAS experiment

The ATLAS[1] detector is the larger one of the two general-purpose detectors located at LHC, the other one being CMS. It is built in multiple modules that each serve a specific purpose. The following sections aim to give a brief overview of the different parts of the ATLAS detector and how they measure physical observables. A schematic view of the detector can be seen in fig. 3.2.

3.2.1 Coordinate system

The coordinate system in ATLAS is a right-handed coordinate system with its origin in the point of collision. The z-axis points in the direction of the beam, the y-axis points upwards and the x-axis points to the center of the LHC ring. Because of the rotationally symmetric setup of the experiment, usually a polar coordinate system is used. ϕ has a range of $[-\pi, \pi]$ and describes the angle around the z-axis and θ is the off-axis angle ranging from 0 to π. A useful observable for particles is the lorentz-invariant *rapidity*, defined as

$$y = \frac{1}{2} \ln \left(\frac{E + p_z}{E - p_z} \right) \tag{3.1}$$

where E is the energy and p_z is the momentum in z-direction. In the limit where the momentum of the particle is much larger than its mass, the rapidity can be approximated by the *pseudorapidity*

$$\eta = -\ln \left[\tan \left(\frac{\theta}{2} \right) \right] \tag{3.2}$$

where θ is the polar angle of the particle's momentum in the usual coordinate system. The pseudorapidity takes values from $-\infty$ to ∞ where large absolute values correspond to momenta which point in a direction close to the z-axis and $\eta = 0$ corresponds to a momentum perpendicular to the z-axis. Usually η is used instead of θ. As a measure for spatial distance between two objects

$$\Delta R = \sqrt{(\Delta\phi)^2 + (\Delta\eta)^2} \tag{3.3}$$

[1] **A** **T**oroidial **L**HC **A**pparatu**S**

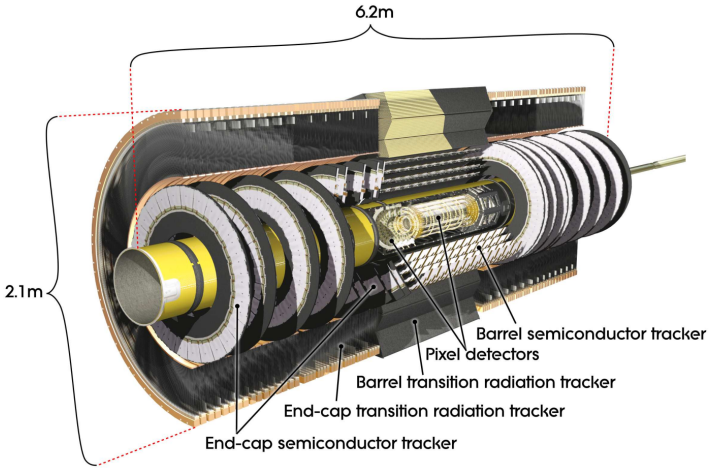

Figure 3.3: The inner detector of ATLAS [37].

is used. In addition to the momentum p, the momentum's projection onto the plane perpendicular to the beam axis, the *transverse momentum* p_{T}, is introduced (see also sec. 5.1.7)

$$p_{\mathrm{T}} = \sqrt{p_x^2 + p_y^2}. \tag{3.4}$$

3.2.2 The inner detector

The inner detector records the tracks of charged particles with a transverse momentum $p_{\mathrm{T}} > 0.5\,\mathrm{GeV}$ with high momentum resolution. Its structure is shown in fig. 3.3. Due to the high density of tracks passing through the detector, it is essential that the spatial resolution is high enough to still be able to distinguish tracks that are close to each other. This is provided by the insertable B-layer (IBL) detector [39], the pixel detector [40] and the silicon microstrip trackers (SCT) [41], which are located in the close vicinity of the nominal interaction point. With approximately 80.4 million readout channels the pixel detector has an extremely high granularity and can for example be used to identify the location of the primary and secondary vertices [37]. The identification of the primary vertex gets improved by an additional layer of 26880 pixel cells in the IBL which is located at a radius of 33 mm around the beam pipe [39] (not shown in fig. 3.3). The SCT helps with tagging heavy-flavour quarks and τ-leptons. Together, the pixel detector and SCT cover a region of $|\eta| < 2.5$. To further follow the tracks, they are surrounded by the transition radiation tracker (TRT) [42] which consists of multiple layers of drift tubes. The TRT further improves the momentum resolution and ability to identify electrons in the range $|\eta| < 2.0$. The whole inner detector is embedded into a 2 T strong magnetic field to bend the tracks of charged tracks and to thus make it possible to determine the sign of the charge of any passing particle [37].

3.2.3 The calorimeters

The calorimeter systems of ATLAS are placed around the inner detector and cover a very wide region of $|\eta| < 4.9$. They are meant to stop electrons and photons (electromagnetic calorimeter) and hadrons (hadronic calorimeter) in their tracks and measure their energy. Because the calorimeter system covers such a large region of η, it is possible to measure most of the missing transverse energy $E_{\mathrm{T}}^{\mathrm{miss}}$ with it (the rest is measured with the inner detector, see sec. 5.1.7). The calorimeter is divided into two parts.

Electromagnetic calorimeter

The electromagnetic calorimeter (ECAL) consists of alternating layers of lead and liquid argon (LAr) detectors, called *sampling* calorimeter. When highly energetic electrons or photons pass through the lead they cause showers of particles to erupt. The size of the particle cascade is proportional to the energy of the original particle, which can be measured in the LAr detectors. The prominent feature of this kind of energy measurement is that the uncertainty gets smaller the larger the energy of the incoming particle is. The thickness of the ECAL is optimized to stop all electrons and photons completely, thus providing an excellent energy measurement for both electrons and photons as well as a way to identify them [37]. The uncertainty on the energy measured by the ECAL was found to be $\frac{\sigma(E)}{E} = \frac{10\,\%\cdot\sqrt{\mathrm{GeV}}}{\sqrt{E/\,\mathrm{GeV}}} + 0.5\,\%$ [43].

Hadronic calorimeter

The hadronic calorimeter (HCAL) stops all strongly interacting particles and measures their energy deposit. This is done by three different parts: The tile calorimeter, the LAr hadronic end-cap calorimeter and the LAr forward calorimeter. The tile calorimeter is a sampling calorimeter made of steel and scintillating tiles. The two LAr calorimeters use copper and tungsten as absorber material interspersed with LAr detectors. Together, they cover the full range of $|\eta| < 4.9$ and prevent any SM particle other than neutrinos or muons from passing through them, the exception being so called *punch-through jets* that have too much energy to be stopped completely by the HCAL. At a granularity of $\Delta\phi \times \Delta\eta = 0.1 \times 0.1$ in the first two layers of the tile calorimeter, the spatial resolution is good enough to be able to use the HCAL to reconstruct jets (see sec. 5.1.4). The energy scale resolution is about 4 % [44].

3.2.4 The muon spectrometers

Except for punch-through jets and neutrinos, only muons enter the muon spectrometers. The muon spectrometers aim to record the tracks of the muons and measure their momenta. Neutrinos cannot be detected because the probability of them interacting with the detector material is too small.

Just like the inner detector, the whole muon spectrometer system is embedded inside a magnetic field to deflect the tracks of the muons with a bending power varying from 1.5 Tm up to 7.5 Tm depending on η. The tracks are recorded by monitored drift tubes (MDT) and cathode strip chambers (CSC) for larger pseudorapidities, covering a total range of $|\eta| < 2.7$. In addition, two types of detectors are installed to trigger muons. These are the resistive plate chambers (RPCs) in the barrel region and the thin gap chambers (TGCs) in the end-cap regions. Each of those consists of multiple layers to be able to require a coincidence of the hits with the track of a muon and suppress erroneous trigger events caused by scattered electrons [37].

3.2.5 The trigger system

At more than one billion collisions per second happening, it is not possible to record all collisions with the ATLAS detector. Instead of trying to record and store every bit of information, the ATLAS detector has a sophisticated system of triggers built in, which select events that promise to contain interesting physics, and discard others.

First, a trigger based on the hardware in the calorimeter, the muon systems and, to some extent, the inner detector (L1 trigger [45]) applies a coarse but extremely fast selection at an

acceptance time of 2.5 μs, reducing the event rate to approximately 10 kHz [45]. It triggers on the appearance of electrons, photons, taus, jets, muons and high missing transverse energy. It is also able to trigger on b-jets using information from the inner detector [46, 47].

Events that passed the L1-trigger are then filtered by the software based high-level trigger (HLT [48]) that further reduces the event rate to 1 kHz. The HLT runs reconstruction algorithms on certain regions of interest defined by the L1 trigger. The trigger decisions made by the HLT are then based on sophisticated selection algorithms based on the reconstructed data [49].

4 Monte Carlo event generation

In order to be able to compare theoretical predictions with observations from the experiment, one needs to simulate the physics processes that are expected to happen in a collider experiment. Because particle collisions are quantum mechanical and thus probabilistic in nature, the method of choice to do this is *Monte Carlo* (MC). MC methods are a general way to construct algorithms that calculate numerical quantities based on pseudorandom[1] numbers that need to follow certain probability distributions.

At the LHC, MC generators are used to generate single pp-collision events that resemble real data when produced in large amounts. The process of generating a "raw" MC event can be split into four stages [50]:

(1) Simulation of the hard scattering process. The cross section is obtained by calculating the matrix element for this process.

(2) Parton showering and hadronisation. This includes soft gluon or photon radiations in the initial and final state (ISR, FSR) as well as strong interactions between colored partons. Colored particles eventually must hadronise to colorless bound states (see sec. 2.1.2 on QCD). This cannot be calculated with perturbative QCD, which is why there are dedicated hadronisation models for this, as described e.g. in ref. [50].

(3) Underlying event. This takes into account soft interactions between the other partons of the colliding protons, resulting in additional parton showers in forward direction.

(4) Decay of shortlived particles. Shortlived in this particular context means that the lifetime of a particle is so short that it decays inside the detector.

The generation of these events is then followed by a dedicated simulation of the detector. This includes simulating the response of each detector component to passing particles. The resulting data contains all available information on each participating particle such as four-vectors, charge and mass[2], as well as the detector response. The data obtained from simulating the detector looks the same as real data recorded by the detector and can be used as input for reconstruction algorithms[3] and can thus be used to compare expectations to measured data in the end.

Because some events that may be interesting to an analysis are very unlikely to happen, it is not feasible to just run a simulation of collisions until there is enough statistics for the process of interest. Instead, there are several MC generators designed to accurately simulate specific physical processes [50]. To restore the original cross sections, a statistical weight is applied to each generated event. Furthermore, the number of generated events N_{MC} is then multiplied by a constant factor to scale the apparent amount of generated data to the amount of recorded data that the MC samples are about to be compared to. A measure

[1] The generation of "random" numbers on a computer will always be deterministic and cannot be truly random. This is a feature rather than a problem—it guarantees that any MC experiment is completely reproducable.

[2] Often referred to as *truth-level information* at ATLAS.

[3] The output of the reconstruction algorithms used on MC generated data is called *reco-level information*.

for the amount of recorded data is the integrated luminosity $\mathcal{L}$. It is the instantaneous luminosity L integrated over time:

$$\mathcal{L} = \int L \, \mathrm{d}t. \tag{4.1}$$

The instantaneous luminosity dictates the rate of collisions $\frac{\mathrm{d}N}{\mathrm{d}t}$ happening at a collider experiment with a cross section σ:

$$\frac{\mathrm{d}N}{\mathrm{d}t} = L\sigma. \tag{4.2}$$

At the LHC, the instantaneous luminosity depends on the numbers of protons per bunch N_1 and N_2, the revolution frequency f, the number of bunches N_b and the widths of the bunches in x and y-direction σ_x and σ_y [51]:

$$L = \frac{N_1 N_2 f N_b}{4\pi\sigma_x\sigma_y}. \tag{4.3}$$

The integrated luminosity achieved during Run 2 at ATLAS is $139\,\mathrm{fb}^{-1}$ [52]. The continuation of this analysis will use the full dataset so the MC samples used are scaled to match this luminosity.

4.1 Sample generation

The MC samples used in this analysis were produced with the generators listed in tab. 4.1. Sherpa is a general-purpose event generator. It features the generation of hard scattering

sample	**generator**	**references**
W+jets	Sherpa 2.2.1 / 2.2.2	[53]
Z+jets	Sherpa 2.2.1 / 2.2.2	
diboson	Sherpa 2.2.1 / 2.2.2	
single top	Powheg, Pythia 8	[54, 55]
$t\bar{t}$	Pythia 8	
signal	MadGraph5_aMC@NL, Pythia 8	[56]

Table 4.1: MC generators of the samples used in this analysis.

interaction up to next-to-next-to-leading order precision as well as parton showering and hadronisation. Powheg is a software framework implementing MC methods to generate hard scattering events at next-to-leading order. It does not feature parton showering, however it is designed to work well with dedicated parton showering software. Pythia 8 is again a general-purpose software framework for MC generation. Its advantage regarding usability is that it is packaged in a way that allows to use only parts of it together with other software. In this analysis for example, Pythia 8 is used for the generation of events and parton showers at the same time for the $t\bar{t}$ background, but only for parton showers for the background single top. MadGraph5_aMC@NLO is a program that is able to calculate matrix elements at next-to-leading order precision, generate events and implement parton showers. It is often used to simulate new physics processes. The detector simulation was done by Geant4 [57].

Signal samples were produced for different masses of the Z' and s as presented in fig. 4.1. The mass of the dark matter particle is set to $m_\chi = 200\,\mathrm{GeV}$ in all samples.

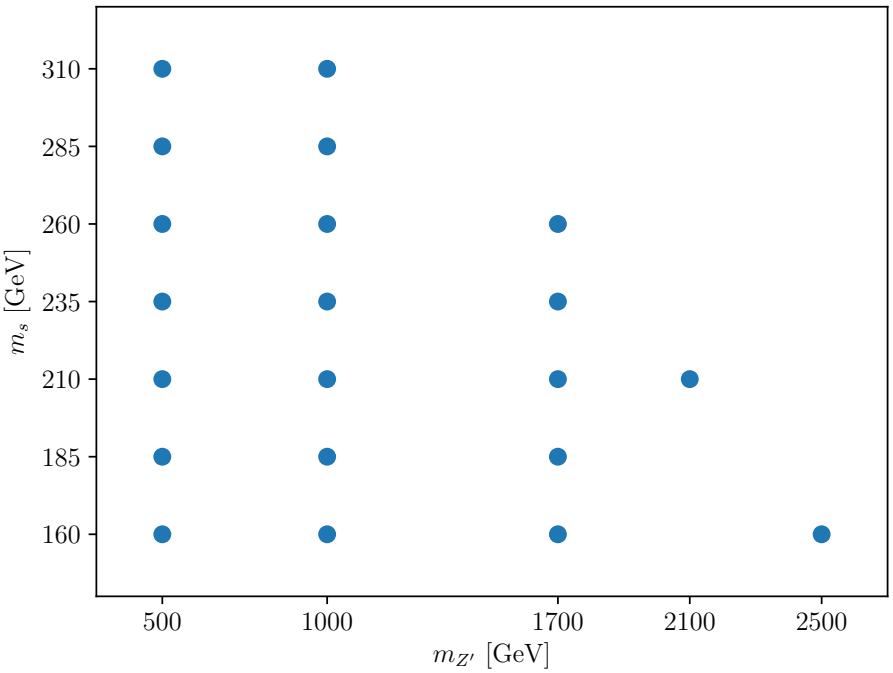

Figure 4.1: Generated signal points. Each dot represents a combination of $m_{Z'}$ and m_s masses for which a MC sample was produced.

5 Reconstruction and event selection

To be able to talk about particles and physical objects in an analysis, the data recorded by the detector or generated by MC needs to be processed so that certain detector signatures can be assigned to particles. The following section discusses how each object that is used in this analysis is reconstructed and defined. Furthermore, not every event is interesting for this analysis. Section 5.2 presents a coarse selection (called *preselection*) of events.

5.1 Object definitions

5.1.1 Electrons

Electrons are identified by leaving energy deposits in the ECAL as well as a track in the inner detector pointing to that cluster. The exact identification is done by considering the shape of the clusters in the ECAL as well as quality criteria on the tracks. More details can be found in ref. [58, 59].

Two levels of strictness exist for electrons: *baseline* and *signal*. The requirements for baseline electrons are a little looser than for signal electrons. The usage of these two levels acknowledges the tradeoff one needs to make between a higher rate of falsely labeling something as an electron and rejecting actual electrons. All electron candidates with $|\eta| > 2.47$ are rejected. Furthermore, electron candidates are required to satisfy $|z_0 \sin\theta| < 0.5\,\text{mm}$ where z_0 is the longitudinal offset of the electron candidate's track to the primary vertex. In addition, the uncertainty in the transverse offset to the primary vertex $\sigma(d_0)$ must be smaller than 5. These selections help to sort out electrons that come from secondary interactions. There are also requirements on the quality of the reconstructed electron, such as a minimum number of two hits in the pixel detector and at least one in the IBL (the exact definition of the used criterion is called `LooseAndBLayerLLH` [58]). To suppress electrons emerging from hadron decays in jets, the energy deposits are also required to be isolated from other activity in the detector. The isolation criterion used in this analysis is called `FixedCutLoose` for both baseline and signal electrons [58]. Baseline electrons are required to have $p_\text{T} > 7\,\text{GeV}$ and signal electrons must have $p_\text{T} > 25\,\text{GeV}$.

5.1.2 Muons

For muon identification, hits in the muon spectrometer, tracks in the inner detector and energy deposits in the ECAL characteristic for a minimum ionizing particle are taken into account [60]. To suppress unwanted noise from the detector, various quality criteria are required for muons. Just like for electrons, two levels of strictness are defined, baseline and signal. All muon candidates must satisfy $|z_0 \sin\theta| < 0.5\,\text{mm}$ and $\sigma(d_0) < 3$. Baseline muons are required to be within $|\eta| < 2.7$ and signal muons in $|\eta| < 2.5$. Baseline muons must have a transverse momentum of $p_\text{T} > 7\,\text{GeV}$. For signal muons, the required transverse momentum is $p_\text{T} > 25\,\text{GeV}$. To suppress muons coming from semileptonic decays in jets, a tighter selection with respect to how isolated the muon is from other activity in the detector is applied to signal muons than to baseline muons. Ref. [60] defines working points for the level of isolation that is required. In this analysis, `LooseTrackOnly` for baseline muons

and `FixedCutTight` for muons is used [60]. In addition, all muon candidates must fulfill certain quality criteria, such as consistency between its momentum as measured in the inner detector and in the muon chambers. Here, the quality requirement `Loose` is applied to baseline muons and `Medium` to signal muons [60].

5.1.3 Taus

Taus typically decay inside the inner detector. Thus taus are reconstructed by looking for jets with certain properties that have their origin in the inner detector (leptonic decays of the tau are not considered). Detailed information on how taus are reconstructed at ATLAS can be found in ref. [61]. Taus in this analysis are required to have $p_{\mathrm{T}} > 20\,\mathrm{GeV}$ and $|\eta| < 2.5$.

5.1.4 Jets

As discussed in sec. 2.1.2, quarks and gluons cannot exist as free particles because of color confinement. Instead, they hadronise. The hadrons that are produced in this way typically move into roughly the same direction as the original quark or gluon, resulting in a cone-shaped particle shower, called *jet*. In the context of a physics analysis, the term "jet" usually refers to the output of a well-defined jet reconstruction algorithm.

There are multiple ways to reconstruct a jet. The standard algorithm used at ATLAS is the anti-k_t algorithm [62]. The main advantage of the anti-k_t algorithm over other jet reconstruction algorithms is that it reconstructs jets that are circular shaped in the ϕ-η plane, which matches our intuition of a cone-shaped jet, and it is infrared and collinear safe, meaning its result does not change significantly if the constituents contain few more or less soft quarks or gluons.

The algorithm is defined like this: First, all distances d_{ij} (see eq. (5.1)) between pairs of input objects i and j and all distances d_{iB} (see eq. (5.2)) between an input object and the beam are calculated. Inputs can be particles, other jets or, in the case of standard jets at ATLAS, calorimeter cells contained in topological clusters.

$$d_{ij} = \min\left(k_{ti}^{-2},\, k_{tj}^{-2}\right) \cdot \frac{\Delta\phi_{ij}^2 + \Delta y_{ij}^2}{R^2} \tag{5.1}$$

$$d_{iB} = k_{ti}^{-2} \tag{5.2}$$

Then, the smallest of these calculated distances is found. If the smallest distance is a distance between two input objects, they are combined and the procedure repeats. Otherwise the smallest distance is one between an input object i and the beam. In this case, i gets removed from the set of inputs and gets called a jet. This repeats until no input objects are left. In the equations (5.1) and (5.2), k_{ti} denotes the transverse momentum of input object i and $\Delta\phi_{ij}$ and Δy_{ij} are the difference in the azimuthal angles and rapidities of objects i and j, respectively. R is a parameter for the algorithm, called the *radius parameter* and it sets the minimal distance[1] two jets reconstructed by this algorithm can have [62].

At ATLAS, the standard for jets is to use the anti-k_t algorithm with a radius parameter of 0.4 on topological clusters in the calorimeters. In this analysis jets are required to have $|\eta| < 2.5$ and $p_{\mathrm{T}} > 20\,\mathrm{GeV}$. To filter out jets coming from secondary interactions, a jet vertex tagger is applied [63].

[1] distance in the ϕ-y-plane

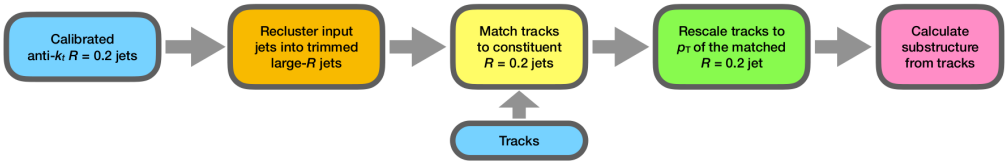

Figure 5.1: Flowchart illustrating the TAR algorithm [64].

Standard large-R jets

To reconstruct jets whose energy deposits are expected to spread over a larger region in the HCAL, the standard radius parameter of $R = 0.4$ is too small. In this analysis, jets with a larger radius parameter are used to reconstruct a hadronically decaying W-boson. They are built with the anti-k_t algorithm with a radius parameter of $R = 1.0$. In further discussions, they are referred to as *large-R jets*. They are required to lie within $|\eta| < 2.0$ and have $p_{\mathrm{T}} > 200\,\mathrm{GeV}$.

Track-assisted reclustered jets

The track-assisted reclustered jet algorithm (TAR) [64] is a novel technique to reconstruct jets. It is designed to provide an improved resolution of the mass and observables linked to the substructure of a jet which might be useful to distinguish jets that emerged from a decaying W-boson from QCD background. The general idea is to make use of the excellent angular resolution of the inner detector of ATLAS. Fig. 5.1 shows a flowchart for the TAR algorithm. Calibrated anti-k_t jets with $R = 0.2$ are provided as input for the anti-k_t algorithm with a larger radius parameter to cluster them into wider jets. Subjets with a p_{T} fraction smaller than $f_{\mathrm{cut}} = 0.05$ are removed from the reclustered jet. Then, the tracks from the inner detector are matched to the subjets under the assumption that each individual track is massless[2]. Each remaining track is matched to the closest subjet if it lies within a given distance. Only one problem remains: The input $R = 0.2$ jets contain neutral components (because they are reconstructed from the calorimeters) while only charged components leave tracks in the inner detector. Because of this, the transverse momenta of the tracks are rescaled to account for the energy of the neutral components using the formula

$$p_{\mathrm{T}}^{\mathrm{track,new}} = p_{\mathrm{T}}^{\mathrm{track,old}} \cdot \frac{p_{\mathrm{T},j}^{\mathrm{subjet}}}{\sum_{i \in j} p_{\mathrm{T},i}^{\mathrm{track,old}}} \tag{5.3}$$

where the sum runs over all tracks that are matched to subjet j. After rescaling, the sum of the transverse momenta of all tracks that belong to a subjet equals the p_{T} of the subjet as measured in the calorimeters, so they can be used to calculate the mass and other substructure variables of the large-R TAR jet [64].

In this analysis, TAR jets with radius parameters $R = 0.6$, $R = 0.8$ and $R = 1.0$ were used. As input jets, calibrated R-scan jets with $p_{\mathrm{T}} > 20\,\mathrm{GeV}$ and $|\eta| < 2.5$ and a radius parameter of $R = 0.2$ are used. R-scan jets are jets reconstructed from topological clusters in the calorimeter using the FastJet [65] implementation of the anti-k_t algorithm. Tracks used as input for the TAR algorithm are required to have a longitudinal offset to the primary vertex of $|z_0 \sin\theta| < 3.0\,\mathrm{mm}$ and a transverse offset of $d_0 < 2.0\,\mathrm{mm}$.

[2] This procedure is called *ghost-association*.

5.1.5 *b*-tagging

Hadrons containing b-quarks (b-hadrons) typically have a rather long lifetime because the decay $b \to Wt$ is kinematically forbidden and the decay $b \to Wc$ is suppressed. As a consequence, b-hadrons decay inside the inner detector and leave very characteristic tracks there at the time of their decay and can thus be distinguished from other signatures. Jets containing a b-hadron are tagged using an algorithm called `MV2c10` which is based on a boosted decision tree (BDT). As an input for the BDT, the outputs of various algorithms are used such as for example a second vertex finding algorithm that reconstructs decay vertices inside jets by locating kinks in the tracks [66]. The parameters of the BDT are tuned in such a way that its efficiency of identifying jets containing b-hadrons is 77 % [67].

5.1.6 Overlap removal

During reconstruction it may occur that the same signatures in the detector are reconstructed multiple times as different objects. To avoid double-counting, *overlap removal* is applied after reconstruction. This is done by defining a set of rules that state in which case an object that shares a track or energy deposit with another object is rejected in favour of the other object. The following rules are applied in this order [29]:

(1) If two electrons share a track, the one with the smaller p_{T} is rejected.

(2) If an electron and a tau lie within a distance of $\Delta R < 0.2$, the tau is rejected.

(3) If a muon that has an energy deposit in the ECAL and an electron share a track, the muon is rejected.

(4) If a muon without any energy deposits in the ECAL and an electron share a track, the electron gets rejected.

(5) If a photon and an electron or muon lie within a distance of $\Delta R < 0.4$, the photon gets rejected.

(6) If a jet and an electron lie within a distance of $\Delta R < 0.2$, the jet gets rejected.

(7) If a jet and an electron lie within a distance of $\Delta R < \min\left(0.4,\ 0.04 + \frac{10\,\mathrm{GeV}}{p_{\mathrm{T}}(e)}\right)$, the electron gets rejected.

(8) If a jet with less than 3 associated tracks and a muon either lie within $\Delta R < 0.2$ or the muon shares a ghost-associated track of the jet, the jet gets rejected.

(9) If a jet and a muon lie within a distance of $\Delta R < \min\left(0.4,\ 0.04 + \frac{10\,\mathrm{GeV}}{p_{\mathrm{T}}(\mu)}\right)$, the muon gets rejected.

(10) If a jet and a tau lie within a distance of $\Delta R < 0.2$, the jet gets rejected.

(11) If a jet and a photon lie within a distance of $\Delta R < 0.4$, the photon gets rejected.

(12) If a large-R jet and an electron lie within a distance of $\Delta R < 1.2$, the large-R jet gets rejected.

(13) If any lepton and a R-scan jet with radius parameter 0.2 lies within a distance of $\Delta R < 0.2$, the jet gets rejected. Because R-scan jets are used as the input to the TAR algorithm, this rule effectively implements overlap removal for TAR jets of any size.

5.1.7 Missing transverse energy and $E_{\mathrm{T}}^{\mathrm{miss}}$-significance

At a collider experiment the total momentum of the incoming particles is controlled by the experimentalist and thus known very well. Note however that protons are complex composite structures whose partons carry an unknown fraction of the total momentum of the proton[3]. Because of this, the total momentum in z-direction of the incoming partons in any interaction at the LHC is not known. It is however reasonable to assume that the transverse momenta (see eq. (3.4)) of the partons are negligible. Therefore the total transverse momentum must always be zero. Due to the conservation of momentum, the total transverse momentum of all particles after an interaction must also be zero. If this is not the case, then there must have been one or more particles that were not detected. Most of the times, this will be a neutrino, but it could also be a new, non-SM particle. The total transverse momentum of all undetected objects is called *missing transverse momentum*. It is calculated by summing all transverse momenta $\vec{p}_{\mathrm{T},i}^{\,\mathrm{visible}}$ of the detected objects:

$$\vec{p}_{\mathrm{T}}^{\,\mathrm{miss}} = -\sum_i \vec{p}_{\mathrm{T},i}^{\,\mathrm{visible}}. \tag{5.4}$$

The absolute value of the missing transverse momentum is referred to as the *missing transverse energy*:

$$E_{\mathrm{T}}^{\mathrm{miss}} := p_{\mathrm{T}}^{\mathrm{miss}} = \left|\vec{p}_{\mathrm{T}}^{\,\mathrm{miss}}\right|. \tag{5.5}$$

In this analysis, $E_{\mathrm{T}}^{\mathrm{miss}}$ is calculated using reconstructed and calibrated objects as input. For leptons, the baseline selection is applied. For jets, the standard jets with $R = 0.4$ without any additional selection criteria are used. In addition to the objects listed above, a track-based soft term (TST) is included in the calculation. The TST accounts for tracks in the inner detector that do not belong to other objects. These tracks are required to fulfill certain quality criteria and must be associated with the primary vertex to suppress pile-up effects [69].

As a measure for the confidence that $E_{\mathrm{T}}^{\mathrm{miss}}$ is indeed caused by particles that cannot be detected instead of coming from detector inefficiencies and mismeasurements or errors in the reconstruction, the $E_{\mathrm{T}}^{\mathrm{miss}}$-significance $\mathcal{S}$ is introduced. $\mathcal{S}$ is defined as the log likelihood ratio of the hypothesis that the transverse momentum of all invisible particles $p_{\mathrm{T}}^{\mathrm{inv}}$ is zero tested against the hypothesis that it is nonzero [70]:

$$\mathcal{S} = \sqrt{2\ln\left(\frac{\max_{p_{\mathrm{T}}^{\mathrm{inv}}\neq 0} L(\vec{p}_T^{\,\mathrm{miss}}|\vec{p}_{\mathrm{T}}^{\,\mathrm{inv}})}{\max_{p_{\mathrm{T}}^{\mathrm{inv}}=0} L(\vec{p}_T^{\,\mathrm{miss}}|\vec{p}_{\mathrm{T}}^{\,\mathrm{inv}})}\right)}. \tag{5.6}$$

The likelihood L depends on the type and the kinematics of all reconstructed objects in the event. Higher values of $\mathcal{S}$ indicate that events with $E_{\mathrm{T}}^{\mathrm{miss}}$ are more likely to contain invisible particles [70].

5.2 Event selection

Not all events are considered in this analysis. For example, it would not make sense to take events into account with no lepton present since this analysis focuses on the semileptonic decay of two W-bosons in the signal model (see sec. 2.2.1). In general, events that contain the process described by the signal model are referred to as *signal* whereas every other

[3] The momenta of the proton's partons are described by *parton distribution functions* (PDFs), see e.g. ref. [68].

event is called *background*. To reduce the amount of background without rejecting signal, a very coarse preselection is applied in the beginning of the analysis.

As mentioned before, events without a lepton are rejected. In this analysis, only electrons and muons are considered as leptons. Exactly one signal muon and no baseline electron or exactly one signal electron and no baseline muon is required. Events that contain taus are rejected. The signal model contains three particles in the final state that cannot be detected (one neutrino and two dark matter particles). The dark matter particles recoil against the dark Higgs s, thus generating a large amount of $E_{\mathrm{T}}^{\mathrm{miss}}$. Therefore a selection of $E_{\mathrm{T}}^{\mathrm{miss}} > 150\,\mathrm{GeV}$ is applied. This value is expected to be much lower than the $E_{\mathrm{T}}^{\mathrm{miss}}$ that is actually present in a signal event, so that only few signal events are rejected. In addition, it is required that the missing transverse energy trigger fired.

Altough in this thesis only MC generated data is analyzed, it should be noted that all recorded events must satisfy additional requirements (event cleaning). Only data blocks from the good run list (GRL) are used. The GRL rejects luminosity blocks during which performance problems with the experimental setup were reported. To further reduce data affected by technical issues, events that contain noise bursts or readout errors in the ECAL or SCT and incomplete events are rejected [29, 71]. Additionally, at least two tracks must be associated with the primary vertex of every event. The primary vertex is identified as the vertex with the largest sum of squares of transverse momenta of all tracks with $p_{\mathrm{T}} > 0.5\,\mathrm{GeV}$ [29].

6 Analysis

6.1 Signal characteristics

As discussed briefly in sec. 5.2, the signature for the signal model contains one lepton and large missing transverse energy coming from the dark matter particles. The quarks coming from one of the W-bosons will form at least one jet, depending on how much momentum the W boson has. In the rest frame of the W, the two quarks are back-to-back. In the lab-frame, however, the quarks inherit the initial momentum of the W-boson. If the momentum of the W-boson is moderate, the two quarks will go off into separate directions before hadronising and form two separate jets, as drawn in fig. 6.1a. This scenario is referred to as *resolved* [72]. If however the initial momentum of the W is large, the momentum directions of the quarks in the lab-frame will be so close together, that, after hadronisation, it is not possible to reconstruct two seperate jets. Instead the two jets merge into one large jet (see fig. 6.1b). This scenario, referred to as the *merged* scenario, is studied in this analysis.

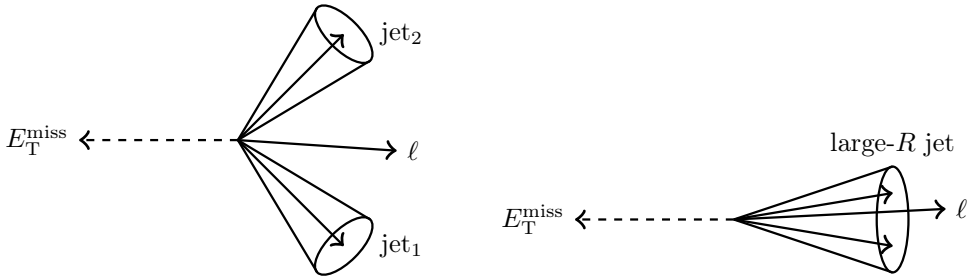

(a) Jet topology in the resolved scenario. **(b)** Jet topology in the merged scenario.

Figure 6.1: Jet topologies in the resolved and merged scenarios.

Naively, it can be expected that the merged scenario occurs more often the heavier the Z' or the dark Higgs s is. If the Z' is very heavy—very heavy meaning here that it is much heavier than the s and the two dark matter particles combined—there is much energy left at its decay to boost the s. A boost of the s would then directly translate into a boost of the two W-bosons, leading to one large jet. If on the other hand the dark Higgs is heavy—that is, much heavier than two W-bosons—the surplus energy at the decay of the s is available to boost the W-bosons, again leading to a merged scenario. This can be seen in fig. 6.2. The plots show the number of large-R jets and TAR jets with $R = 1.0$ for different points on the signal grid. Fig. 6.2a–b show the number of jets for several signal points with fixed $m_s = 160\,\mathrm{GeV}$ and increasing $m_{Z'}$. In both plots it can be seen that more often one large jet is present for larger Z' masses which indicates that the event has a rather merged-like topology. In fig. 6.2c–d again the number of jets is shown, but this time with fixed $m_{Z'} = 1000\,\mathrm{GeV}$ and increasing m_s. Here, the amount of events with a large jet also increases with the mass of the dark Higgs. This observation is consistent with the naive picture of the event topology and its dependence on the masses of the Z' and the dark Higgs. Note that the large difference in the number of events with no jets between large-R jets and TAR jets stems from the fact that large-R jets are required to have a transverse momentum of more than 200 GeV which drastically increases the amount of events with no

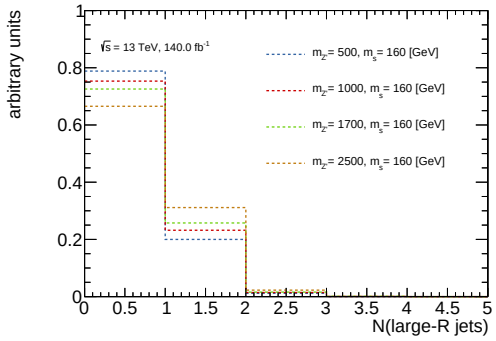

(a) Number of large-R jets for increasing $m_{Z'}$.

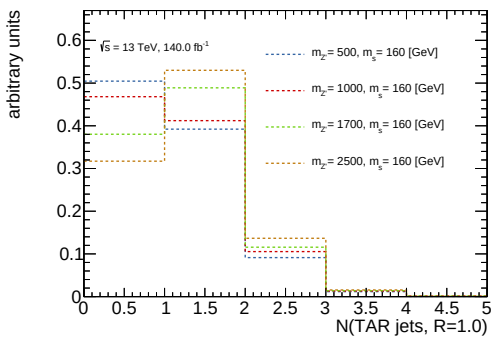

(b) Number of TAR jets for increasing $m_{Z'}$.

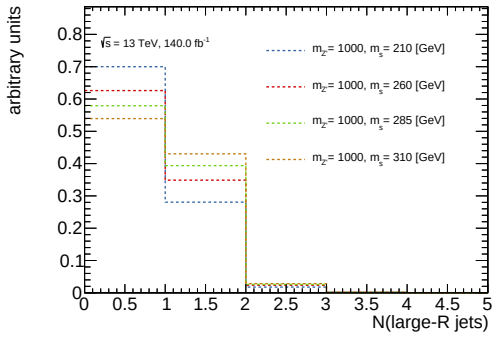

(c) Number of large-R jets for increasing m_s.

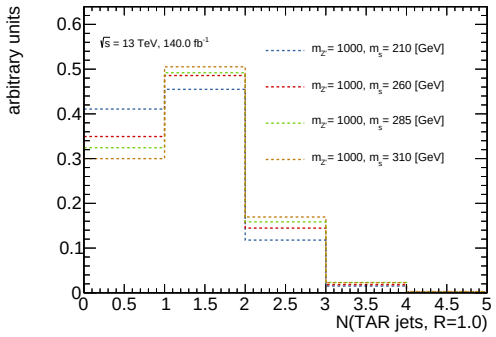

(d) Number of TAR jets for increasing m_s.

Figure 6.2: Dependence of the number of large-R jets and TAR jets with $R = 1.0$ on the masses of the Z' and s. Subfigures a–b show the number of jets for several signal points with fixed $m_s = 160\,\text{GeV}$ and increasing $m_{Z'}$. Subfigures c–d show the number of jets with fixed $m_{Z'} = 1000\,\text{GeV}$ and increasing m_s. All plots are normalized to unit-area.

large-R jets present.

To define a candidate for the hadronically decaying W-boson in the merged scenario it is necessary to reconstruct a jet with a large enough radius parameter to capture all its components. The following section discusses which jet reconstruction method fits best for this task.

6.2 Comparison of different large-R jets

In sec. 5.1.4 various ways to reconstruct a jet were presented. The standard at ATLAS is to use anti-k_t jets with $R = 0.4$. This radius parameter however is too small to reconstruct a W-boson candidate well in the merged scenario (see discussion below). The other possibilities, especially for larger jets, are to use either anti-k_t jets with $R = 1.0$ or the novel TAR jets with a large radius parameter. In this section, the following jet-collections are compared: standard jets with $R = 0.4$, TAR jets with $R = 0.6$, TAR jets with $R = 0.8$, TAR jets with $R = 1.0$ and standard jets with $R = 1.0$ (large-R jets). The metric to decide which kind of jet reconstructs the W best is how close the mass of the jet with the highest p_T (the *hardest* jet) in a given jet-collection is to the mass of the W-boson. Fig. 6.3 shows the mass distributions of the jet-collections listed above for different signal points. For all plotted signal points the mass of the Z' is 1000 GeV, while the mass of the dark Higgs boson m_s ranges from 210 GeV to 310 GeV. First of all, it can be seen in fig. 6.3a that the mass

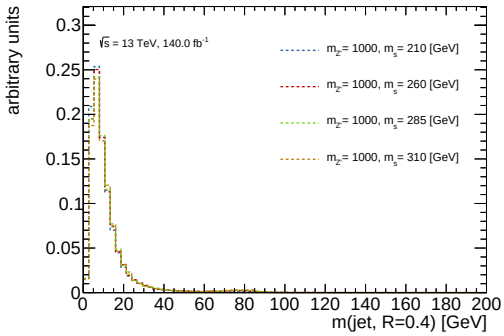

(a) Mass of the hardest standard $R = 0.4$ jet.

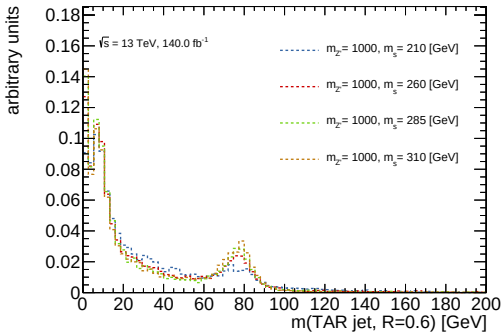

(b) Mass of the hardest $R = 0.6$ TAR jet.

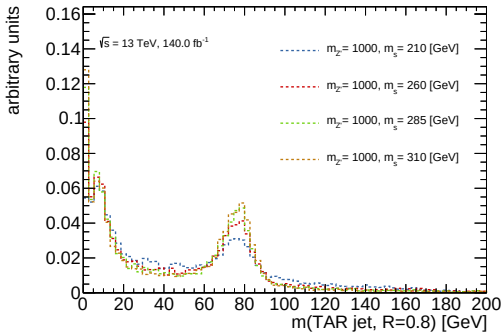

(c) Mass of the hardest $R = 0.8$ TAR jet.

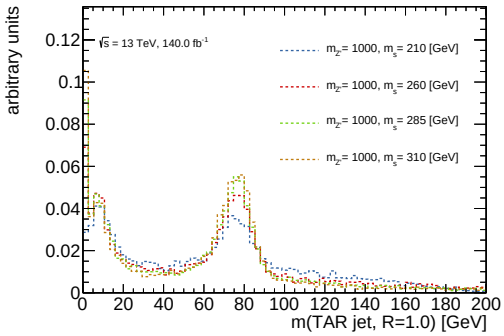

(d) Mass of the hardest $R = 1.0$ TAR jet.

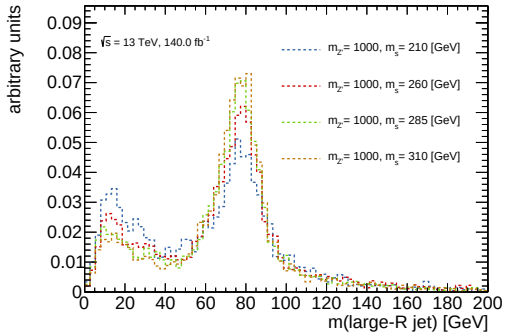

(e) Mass of the hardest large-R jet.

Figure 6.3: Mass distribution of the hardest standard $R = 0.4$ jet (fig. 6.3a), TAR jet with $R = 0.6$ (fig. 6.3b), $R = 0.8$ (fig. 6.3c), $R = 1.0$ (fig. 6.3d) and large-R jet (fig. 6.3e) for different signal points with fixed $m_{Z'} = 1000\,\text{GeV}$ and various dark Higgs masses. All distributions are normalized to unity.

distribution of the hardest standard $R = 0.4$ jet does not peak at all at the W-mass. This shows that using this reconstruction technique for jets never reconstructs the hadronically decaying W-boson and justifies the need for jets with a larger radius parameter. The other plots in fig. 6.3 show that the mass distributions peak more clearly the higher the mass of the dark Higgs is. This again supports the idea that larger dark Higgs masses lead to a rather merged-like event topology.

The mass distribution of the TAR jets with $R = 0.6$ (fig. 6.3b) shows only a little bump at the W-mass for signal points with higher values of m_s, while for lower dark Higgs masses there is no clear peak at all. For TAR jets with $R = 0.8$ and $R = 1.0$ (fig. 6.3c–d) the

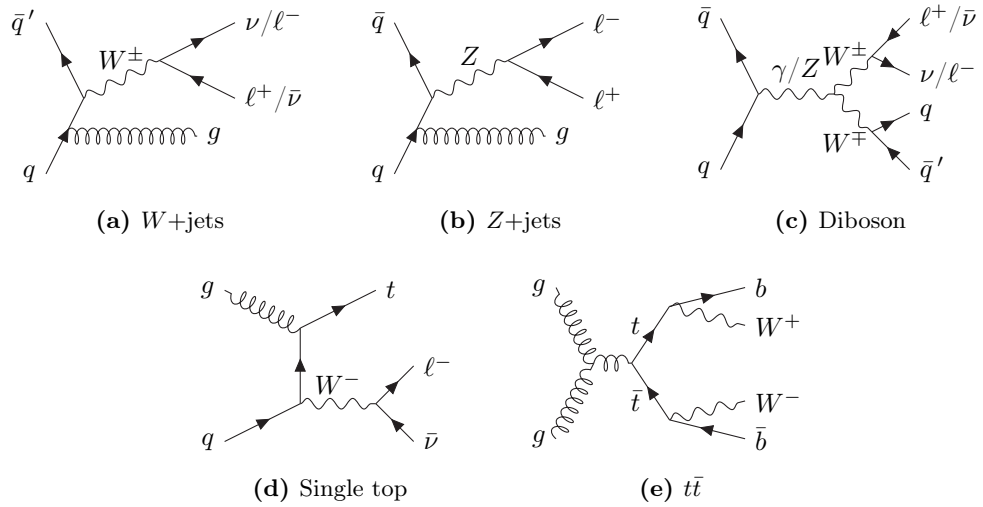

(a) W+jets **(b)** Z+jets **(c)** Diboson

(d) Single top **(e)** $t\bar{t}$

Figure 6.4: Examples of Feynman diagrams contributing to the background processes of the signal model.

peak is more pronounced. The mass distribution of the large-R jets, however, peaks far more clearly for all tested signal points than it does for any of the TAR jets. This shows that large-R jets are better suited for reconstructing the hadronically decaying W-boson in a merged scenario than the TAR jets, which were originally introduced because of their promising features related to boosted W-decays.

6.3 Optimization of the signal region

The selection criteria presented in sec. 5.2 suppress background events only very limited with respect to the signal. In order to be sensitive to a signal, finer criteria must be defined that select signal events while leaving very little background events. In this section the backgrounds that are relevant for the signal model are presented. Then an optimization of the selection criteria defining the signal region to suppress backgrounds is shown. Finally, a cross-check and validation for the optimized signal region is performed.

6.3.1 Backgrounds

In general, all processes that lead to one lepton, missing transverse energy and a large-R jet being reconstructed constitute background events to the signal. This section discusses SM processes that are still present after applying the preselection presented in sec. 5.2. Note that the preselection does not require the presence of a large-R jet, so even processes with no large jets or even no jets at all can pass the preselection. Fig. 6.4 shows one Feynman diagram for each process that contributes to the discussed backgrounds.

W+jets

This background comes from events that contain a W-boson that decays leptonically. The decay products of the W contribute one lepton and missing transverse energy. One or more jets may be coming from ISR. A Feynman diagram that contributes to this process is shown in fig. 6.4a.

Z+jets

Events that contain a Z-boson may also contribute to the background for this signal. If the Z decays leptonically but one of the leptons is not within the geometrical acceptance of the detector or gets misidentified, the resulting signature has only one lepton and matches the preselection. If on the other hand the Z decays hadronically, but there is one fake lepton, the signature resembles the signal. Additional jets again can come from ISR (see fig. 6.4b).

Diboson

Diboson backgrounds include all processes that contain two weak bosons, that is WW, WZ and ZZ. In the case where one leptonically decaying W-boson is present and the other boson decays hadronically, the signature of the signal is imitated (see fig. 6.4c). Similar to Z+jets, ZZ only passes the preselection criteria if one lepton gets misidentified or missed.

Single top

Processes where a single top quark gets produced are referred to as "single top". In particular the production of a top quark in association with a W-boson can resemble the signal if the W decays into a charged lepton and a neutrino (see fig. 6.4d). The decay of the top quark leads to the presence of several jets, where one of the jets typically contains b-hadrons. In another scenario, the W that is produced together with the t-quark decays hadronically and the W coming from the t decays into a charged lepton and a neutrino, in which case the signature is again similar to the signal [73].

$t\bar{t}$

Events where a top-antitop quark pair gets produced are called $t\bar{t}$. A (anti-) top quark almost always decays into a W-boson and a (anti-) b-quark (see fig. 6.4e). Because the signal model also contains two W-bosons, this process contributes to the background [74].

6.3.2 Optimization

To reduce the amount of background, a set of selection criteria needs to be optimized for the signal region. Because the topology of the signature is quite different for the resolved and merged scenario (see sec. 6.1), it is not promising to look for criteria that select events from both the resolved and merged region simultaneously. Therefore, two dedicated signal regions are defined, one for the resolved and one for the merged region. The optimization of the resolved region is presented in ref. [75]. In this analysis, the selection criteria for the merged scenario were optimized.

The optimization was performed with respect to the expected significance Z. A more detailed discussion on the significance is given in sec. 6.4. For now, it should be sufficient to say that this optimization tries to maximize Z. In this optimization, the Asimov-significance was used:

$$Z = \sqrt{2\left[\ln\left(\frac{(s+b)(b+\sigma_b^2)}{b^2+(s+b)\sigma_b^2}\right) - \frac{b^2}{\sigma_b^2}\ln\left(1+\frac{\sigma_b^2 s}{b(b+\sigma_b^2)}\right)\right]} \tag{6.1}$$

where s is the expected number of signal events, b is the expected number of background events and σ_b is the statistical uncertainty on the expected number of background events.

The optimal signal region definition was found by repeatedly creating so called n-1-plots of all variables that promise to have a suppressing effect on the background. A n-1-plot shows the distribution of a variable where all previously defined selection criteria are applied

variable	requirement
number of large-R jets	> 0
number of b-jets	$= 0$
$E_{\mathrm{T}}^{\mathrm{miss}}$	$> 300\,\mathrm{GeV}$
m_{T}	$> 150\,\mathrm{GeV}$
$m_{\text{large-}R\text{ jet}}$	$> 60\,\mathrm{GeV}$ and $< 100\,\mathrm{GeV}$
$\mathcal{S}$	> 15
$\Delta R(\ell,\ \text{large-}R\text{ jet})$	< 1.6
$D_2^{\beta=1}$	< 1.4

Table 6.1: Optimized selection criteria for the signal region in the merged scenario. These are applied in addition to the preselection defined in sec. 5.2.

except the one regarding the shown variable. This way it is possible to see how a given distribution behaves under the applied selection. To decide which requirement on that variable would maximize Z, the n-1-plot contains a panel indicating the expected significance that would result in cutting at each value. Because introducing a new requirement affects the distribution of all other variables, each previously defined selection criterion needs to be checked and, if necessary, readjusted after every change. This process is repeated until the requirements on every variable are located at a value that maximizes Z. The optimization was performed on three signal samples that are expected to lie in the merged region: two with $m_{Z'} = 1000\,\mathrm{GeV}$ and $m_s = 260\,\mathrm{GeV}$ or $m_s = 310\,\mathrm{GeV}$ and one with $m_{Z'} = 1700\,\mathrm{GeV}$ and $m_s = 260\,\mathrm{GeV}$. The analysis and visualization of the samples was performed using the data analysis framework ROOT [76].

The selection criteria that were found to achieve the highest expected significance for the three probed signal points are listed in tab. 6.1. Since some variables are based on the properties of the hardest large-R jet, naturally the requirement that at least one large-R jet is present was introduced before the optimization.

In the following all variables used in tab. 6.1 that have not been introduced so far are explained and the choice of each value is justified.

Number of *b*-jets

The large-R jet characteristic for the merged topology of the signal signature comes from a hadronically decaying W-boson. The decay $W^+ \to t\bar{b}$ or $W^- \to \bar{t}b$ is kinematically forbidden because the top quark is much heavier than the W-boson. All other decays of the W into a b-quark are extremely unlikely [8]. Thus, it is well-motivated to require that no b-tagged jets are present. This requirement is particularly useful to suppress $t\bar{t}$ and single top background, since their signatures typically contain one or two b-jets. The number of b-jets after the preselection is applied is shown in fig. 6.5a. All distributions shown after preselection are normalized to unit-area. It can be seen that especially for $t\bar{t}$ and single top most events have one or more b-jet, while the signal contains rarely any b-jets. Fig. 6.5b shows the corresponding n-1-plot where all selection criteria are applied except the one on the number of b-jets itself. The requirement on the number of b-jets is indicated by the black vertical line and the arrow. It can be clearly seen that this requirement is very effective in rejecting backgrounds that contain top-quarks. It has been shown that the b-veto alone reduces the expected number of $t\bar{t}$ events by a factor of about 0.12 and the number of single top events by a factor of about 0.71. The exact values of the expected number of background events after each cut are listed in tab. 6.2.

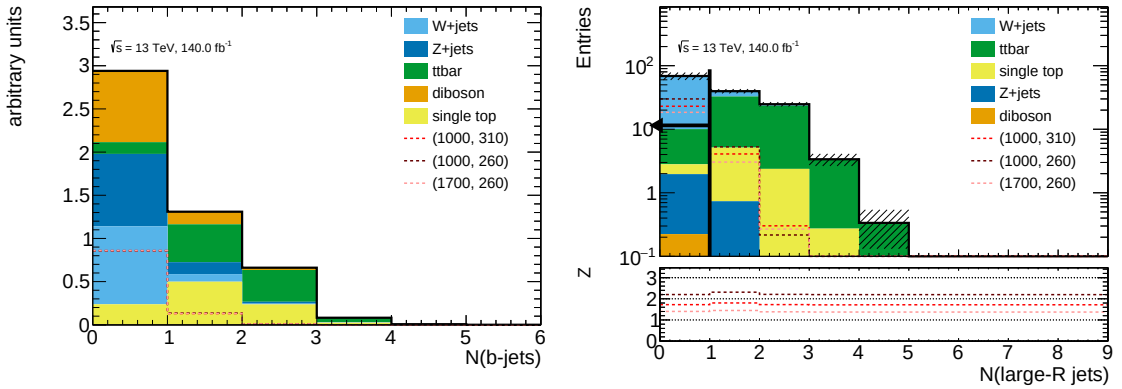

(a) Number of b-jets after preselection. **(b)** N-1-plot for the number of b-jets.

Figure 6.5: Distribution and n-1-plot of the number of b-jets. The labels of the signal samples indicate the masses of the Z' and dark Higgs $(m_{Z'}, m_s)$ in GeV.

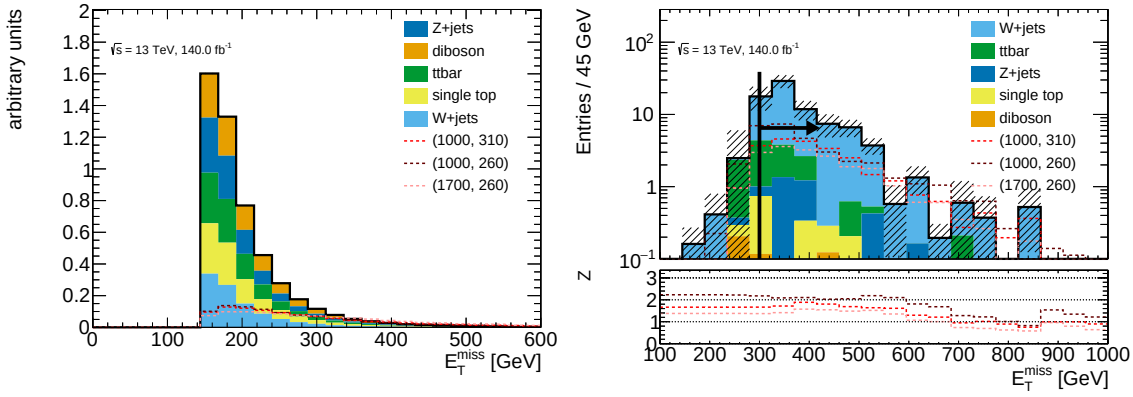

(a) $E_{\mathrm{T}}^{\mathrm{miss}}$ after preselection. **(b)** N-1-plot for $E_{\mathrm{T}}^{\mathrm{miss}}$.

Figure 6.6: Distribution and n-1-plot of $E_{\mathrm{T}}^{\mathrm{miss}}$.

$E_{\mathrm{T}}^{\mathrm{miss}}$

A requirement of high $E_{\mathrm{T}}^{\mathrm{miss}}$ is meant to move the entire topology towards a rather boosted regime and thus selecting events that belong to the merged scenario. In addition, it has in general a suppressive effect on all backgrounds, since in SM processes the missing transverse energy generated by neutrinos is less than expected from escaping dark matter particles. Fig. 6.6a and b show the distribution and the n-1-plot for $E_{\mathrm{T}}^{\mathrm{miss}}$. From the panel below the n-1-plot it can be seen that there is no clear maximum of Z. The minimal requirement of 300 GeV for $E_{\mathrm{T}}^{\mathrm{miss}}$ was chosen as the maximal value where Z is consistently high for all three signal points shown in the plot. For higher values of $E_{\mathrm{T}}^{\mathrm{miss}}$ the expected significance gets inconsistent between the three signal samples and then slowly decreases.

Transverse mass

The transverse mass, defined as

$$m_{\mathrm{T}} = \sqrt{2 p_{\mathrm{T}}^{\ell} E_{\mathrm{T}}^{\mathrm{miss}} \left(1 - \cos\Delta\phi\left(\ell, \vec{p}_{\mathrm{T}}^{\,\mathrm{miss}}\right)\right)}, \tag{6.2}$$

using the missing transverse energy and the lepton ℓ, was originally introduced to help reconstruct the mass of the W-boson [77] and is now widely used in searches for new physics

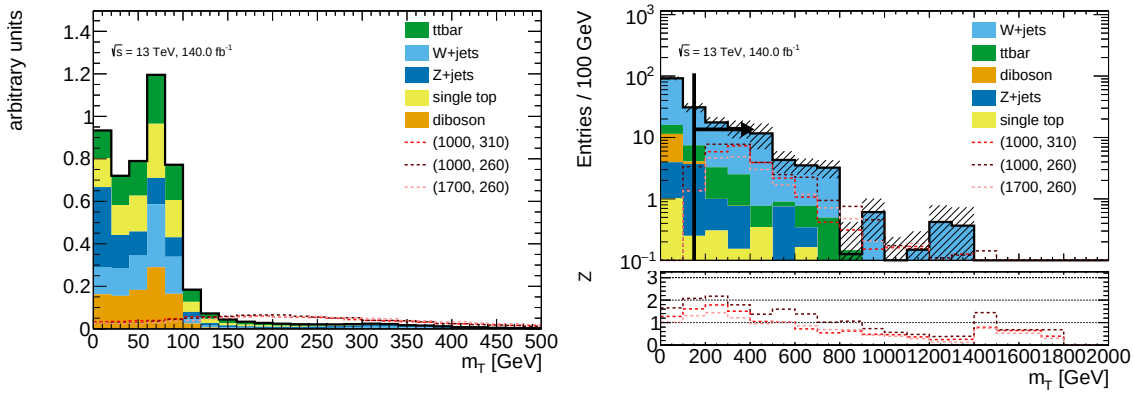

(a) m_{T} after preselection.

(b) N-1-plot for m_{T}.

Figure 6.7: Distribution and n-1-plot for m_{T}.

to reduce $t\bar{t}$ and W+jets background [78]. Fig. 6.7a shows the distribution of the transverse mass after the preselection was applied. The SM processes that contain W-bosons nicely peak right below 80 GeV, the mass of the W-boson. For the signal, m_{T} takes much higher values which makes it a promising variable to suppress background. The n-1-plot for m_{T} is shown in fig. 6.7b. It can be seen that the proposed selection at $m_{\mathrm{T}} > 150$ GeV rejects large parts of the W+jets, Z+jets and diboson backgrounds, while discarding very little signal. The criterion on m_{T} also lies on a maximum of the expected significance, seen in the panel below the histogram. The bump in Z at around 1500 GeV comes from statistical fluctuations in the MC simulation and is not reliable.

Mass of the large-R jet

As discussed in sec. 6.2, the large-R jet is meant to reconstruct the hadronically decaying W-boson. Therefore, it is required that the mass of the hardest large-R jet approximately equals the mass of the W-boson which is roughly 80 GeV (see eq. (2.16)). The distribution of the mass can be seen in fig. 6.8a. The signal as well as the SM processes peak at the W-mass. However, the signal hardly contains any large-R jets with a small mass whereas the SM does. The mass-window that was found to work best for this analysis is $60\,\mathrm{GeV} < m < 100\,\mathrm{GeV}$. The related n-1-plots are shown in fig. 6.8b–c. Both selection criteria are chosen in such a way that they maximize Z.

Missing transverse energy significance

The distribution of $\mathcal{S}$ is shown in fig. 6.9a. All SM processes behave mostly consistent and peak at $\mathcal{S} \approx 10$. The $E_{\mathrm{T}}^{\mathrm{miss}}$ significance of the signals shown here clearly shift to higher values than the SM. The requirement on the $E_{\mathrm{T}}^{\mathrm{miss}}$ significance $\mathcal{S} > 15$ is mainly used to further suppress background. It does also reject signal, so the expected significance increases only very slightly, as can be seen in fig. 6.9b. However, since high values of $\mathcal{S}$ increase the confidence that the $E_{\mathrm{T}}^{\mathrm{miss}}$ indeed comes from invisible particles, it makes sense to introduce this requirement in interplay with the requirement on high values of $E_{\mathrm{T}}^{\mathrm{miss}}$.

Distance between the lepton and the large-R jet

If the dark Higgs s is strongly boosted, not only the hadronically decaying W-boson is boosted, but the leptonically decaying one also. Analogous to the argumentation that the two quarks from a boosted W-boson should merge into a large-R jet due to being close

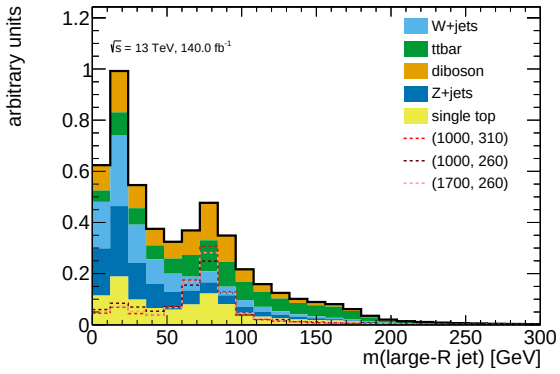

(a) m(large-R jet) after preselection.

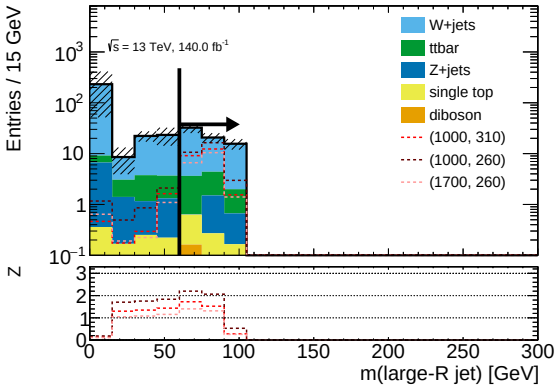

(b) Lower requirement on the jet-mass.

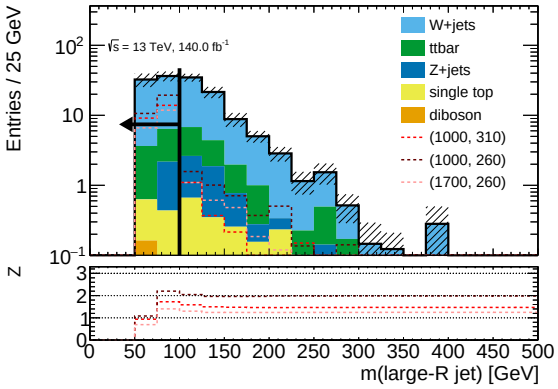

(c) Upper requirement on the jet-mass.

Figure 6.8: Distribution and n-1-plots for the mass of the hardest large-R jet.

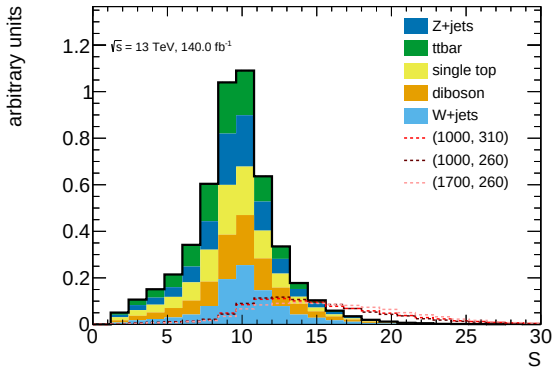

(a) $\mathcal{S}$ after preselection.

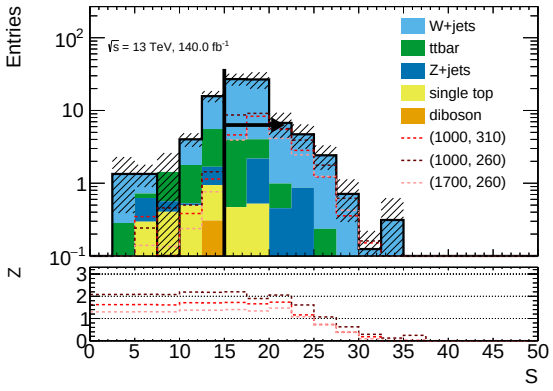

(b) N-1-plot of $\mathcal{S}$.

Figure 6.9: Distribution and n-1-plot of the $E_{\mathrm{T}}^{\mathrm{miss}}$ significance.

together, the two W-bosons coming from a boosted s—and thus their decay products—should also lie rather close together. The visible decay products of the two W-bosons are the large-R jet and the lepton (referred to as j and ℓ for shortness in the formula below). Their distance is calculated via

$$\Delta R(\ell, j) = \sqrt{\Delta\phi^2(\ell, j) + \Delta\eta^2(\ell, j)}. \tag{6.3}$$

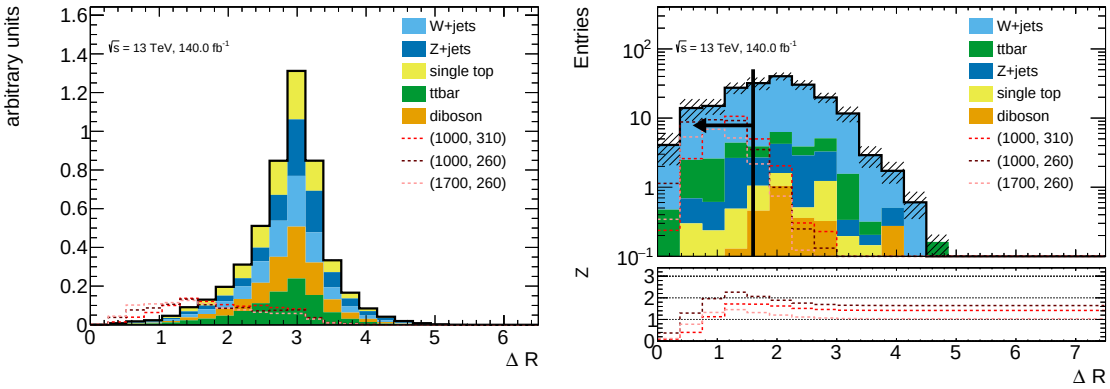

(a) $\Delta R(\ell, j)$ after preselection. **(b)** N-1-plot for $\Delta R(\ell, j)$.

Figure 6.10: Distribution and n-1-plot of ΔR between the lepton and the hardest large-R jet.

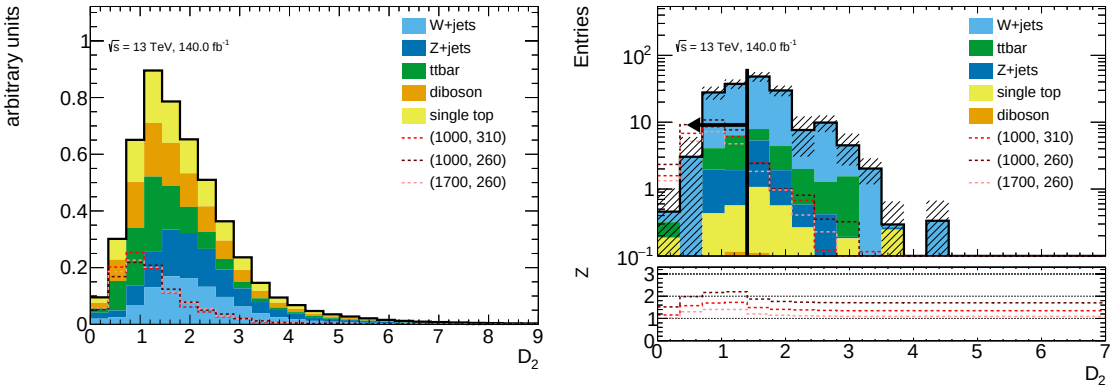

(a) $D_2^{\beta=1}$ after preselection. **(b)** N-1-plot for $D_2^{\beta=1}$.

Figure 6.11: Distribution and n-1-plot for $D_2^{\beta=1}$.

As can be seen in fig. 6.10a, the distributions of $\Delta R(\ell, j)$ look quite different for signal and background. For SM processes, ΔR peaks around 3, so close to π. This means that for SM processes, the hardest large-R jet and the direction of $E_{\mathrm{T}}^{\mathrm{miss}}$ typically lie back-to-back. For the signal, the values of ΔR are shifted to smaller values as expected (see sec. 6.1). As can be seen in fig. 6.10b, the clear peak in the distribution of the backgrounds vanishes under the applied signal region selection. The distributions of $\Delta R(\ell, j)$ look quite different for the three signal points. This is expected as they all have different masses of the dark Higgs which directly influences the topology of the signature. The requirement $\Delta R(\ell, j) < 1.6$ compromises between the three signal points.

$D_2^{\beta=1}$

The variable $D_2^{\beta=1}$ is a ratio of energy correlation functions [79] calculated from the energies and angular distances of the particles contained in the large-R jet. $D_2^{\beta=1}$ is optimized to distinguish between QCD jets and jets that come from a hadronically decaying boosted W-boson [80]. The exact definition can be found in ref. [81]. Small values of $D_2^{\beta=1}$ mean that a jet is more likely to be the result of a W-decay than from some QCD process. In fig. 6.11a it can be seen that $D_2^{\beta=1}$ looks similar for signal and background, however for the signal, the values of $D_2^{\beta=1}$ tend to slightly smaller values. Fig. 6.11b shows the n-1-plot

for this variable. It can be clearly seen that introducing a requirement on it improves the expected significance.

Other variables

Besides the variables discussed above, also the p_{T} of the lepton, the p_{T} of the large-R jet and a jet substructure variable called τ_{21} was tried in the optimization. τ_{21} is defined as the ratio $\frac{\tau_2}{\tau_1}$ where τ_N is a measure for the likeliness that a large-R jet is best described by having N subjets. Typically, jets caused by W-decays have a lower τ_{21} than QCD jets [80]. It turned out, however, that none of these variables show a discriminating power over the background so no further requirements were introduced.

Background yields in the signal region

Tab. 6.2 shows the expected number of background events in the signal region. The total number of background events gets significantly reduced by the selection presented above, leaving a total of 67.79 expected events with an acceptable uncertainty of 13.6 %. W+jets is by far the most prominent background, followed by $t\bar{t}$, as was already visible in the n-1-plots. Of all background processes, diboson has the signature most similar to the signal. The reason diboson is almost entirely eliminated after the selection is applied is mainly due to the requirements on m_{T} and $E_{\mathrm{T}}^{\mathrm{miss}}$ (see tab. 6.2). m_{T} depends on the angular distance between $\vec{p}_{\mathrm{T}}^{\,\mathrm{miss}}$ and the lepton (see eq. (6.2)) in a way such that small angular distances lead to small values of m_{T} and vice versa. Because the lepton and all $E_{\mathrm{T}}^{\mathrm{miss}}$ in the signature of the diboson background comes from one of the W or Z-bosons decaying leptonically, the direction of the missing transverse momentum and the lepton is typically rather close together and thus m_{T} small. This is not the case for the signal, where the $E_{\mathrm{T}}^{\mathrm{miss}}$ comes mainly from dark matter particles that recoil against the visible decay products. Thus, m_{T} is very effective at suppressing diboson processes.

	Total SM	W+jets	Z+jets	Diboson	single top	$t\bar{t}$
preselection	6888722.43 ± 8730.42	4857088.06 ± 8706.18	111868.70 ± 325.78	90088.27 ± 148.50	225149.73 ± 221.26	1603804.50 ± 495.40
$N_j > 0$	3115549.79 ± 1639.79	2072465.59 ± 1583.32	50737.94 ± 149.92	49644.60 ± 108.87	112985.91 ± 153.43	829292.50 ± 352.33
b-veto	2028606.62 ± 1505.73	1828748.40 ± 1489.16	41688.06 ± 142.86	39922.74 ± 99.83	22196.15 ± 67.88	96013.44 ± 120.97
$m_{\mathrm{T}} > 150\,\mathrm{GeV}$	24179.92 ± 362.45	18991.61 ± 360.53	1179.35 ± 27.83	224.54 ± 6.37	544.02 ± 9.15	3240.00 ± 22.16
$E_{\mathrm{T}}^{\mathrm{miss}} > 300\,\mathrm{GeV}$	5630.30 ± 212.01	4632.75 ± 211.33	288.93 ± 13.43	31.18 ± 2.27	121.21 ± 4.24	556.17 ± 9.21
$m_j > 60\,\mathrm{GeV}$	1530.33 ± 30.91	1192.82 ± 29.80	80.88 ± 5.30	17.51 ± 1.71	45.61 ± 2.58	193.48 ± 5.45
$m_j < 100\,\mathrm{GeV}$	785.25 ± 25.31	618.74 ± 24.54	40.44 ± 4.35	9.06 ± 1.33	23.68 ± 1.89	93.31 ± 3.79
$\mathcal{S} > 15$	522.21 ± 21.46	447.40 ± 21.01	27.57 ± 3.42	4.17 ± 0.88	9.47 ± 1.20	33.59 ± 2.26
$\Delta R < 1.6$	168.19 ± 14.39	142.72 ± 14.06	7.72 ± 2.57	0.38 ± 0.20	2.67 ± 0.69	14.70 ± 1.47
$D_2^{\beta=1} < 1.4$	67.79 ± 9.24	58.66 ± 8.95	1.38 ± 2.01	0.22 ± 0.16	0.66 ± 0.35	6.86 ± 0.99
signal region	67.79 ± 9.24	58.66 ± 8.95	1.38 ± 2.01	0.22 ± 0.16	0.66 ± 0.35	6.86 ± 0.99

Table 6.2: Expected number of events for each background after each selection criterion. N_j refers here to the number of large-R jets and m_j to the mass of the hardest large-R jet. The event numbers are given with their statistical uncertainty.

6.3.3 Cross-check of possible selections

The method presented above gives convincing arguments that the chosen signal region makes sense for the merged scenario and is promising to yield a good expected significance. It fails however to show that this selection is the best possible way to define the signal region. To tackle this, an automated scan over a large set of possible selections was performed using a program called ahoi[1]. First, it calculates the expected number of events for signal and background for every possible selection. To make sure that the results (see discussion below on what kind of results ahoi produces) do not stem from statistical fluctuations, all input samples are randomly split into two subsets before the calculation. From this, a *receiver operator characteristic* (ROC) curve can be created. The x-axis of this ROC curve shows the efficiency of selecting signal ϵ_{signal} ranging from 0 to 1 with 1 corresponding to the case that no signal gets rejected and 0 meaning that no signal is left. The y-axis shows the efficiency of rejecting background $1 - \epsilon_{\text{background}}$ with a value of 1 meaning that no background passes the selection and 0 meaning that no background gets rejected. The goal is of course to reject as much background as possible (and meaningful) while rejecting only few signal events. Ahoi constructs the ROC curve by iterating over all possible combinations of selection criteria for which ϵ_{signal} and $\epsilon_{\text{background}}$ were calculated before. For each value of the signal efficiency that results from a selection, a point with the corresponding background rejection efficiency gets added to the ROC curve. If there are multiple selections leading to the same signal efficiency (within a given range), the one with the larger background rejection gets chosen to appear in the ROC curve. Thus the ROC curve only contains points where the background rejection is maximal for any given signal efficiency. The user interface of ahoi then allows to query which combination of selection criteria lead to a specific point on the ROC curve. Furthermore it is easy to calculate an expected significance using eq. (6.1) for every reached signal efficiency, resulting in a *significance scan* plot.

In this analysis, ahoi was used with two goals: first, verify that the choice of the signal region presented in sec. 6.3.2 is among the best possible choices and second, verify that the choice of using large-R jets and not TAR jets is justified in terms of the expected significance that can be achieved.

The optimization with ahoi was performed on the signal point with $m_{Z'} = 1000\,\text{GeV}$ and $m_s = 260\,\text{GeV}$[2]. The set of selections consisted of wide ranges of requirements on all variables used to define the signal region in sec. 6.3.2 and additional requirements on the p_{T} of the lepton, the p_{T} of the leading large-R jet and on τ_{21} resulting in a total of more than $17,000,000$ possible cut combinations (thus the term "brute-force" scan). The ROC curve and significance scan are shown in fig. 6.12. Selections that lead to a statistical uncertainty on the background of more than 30 % were discarded in both plots. First of all, it should be noted that the apparently small values of ϵ_{signal} are not a problem. Large parts of the signal get rejected by requiring just one large-R jet already—after all, the signal region is optimized for the merged scenario only. The ROC curves for both subsets are reasonably smooth and consistent with each other. The corresponding significance scan plot shows values of Z up to 3, however in a region where the signal efficiency is very small and the two subsets are not at all consistent with each other. For signal efficiencies above 0.05 the significance curve gets smoother and the curves for the two subsets grow closer. Between 0.05 and 0.10 the expected significances for both subsets lie between 2 and 1.5. Checking some selections in this region shows mostly consistency with the signal region that was found using the approach discussed in sec. 6.3.2. Most importantly, none of the selections found to be optimal by ahoi contain additional requirements on the p_{T} of the lepton or

[1] Ahoi was written by Dr. Nikolai Hartmann and is available at `https://gitlab.com/nikoladze/ahoi`.

[2] In fact, also optimizations on other signal points in the merged region were performed, they however do not lead to different or new conclusions and are therefore not shown here.

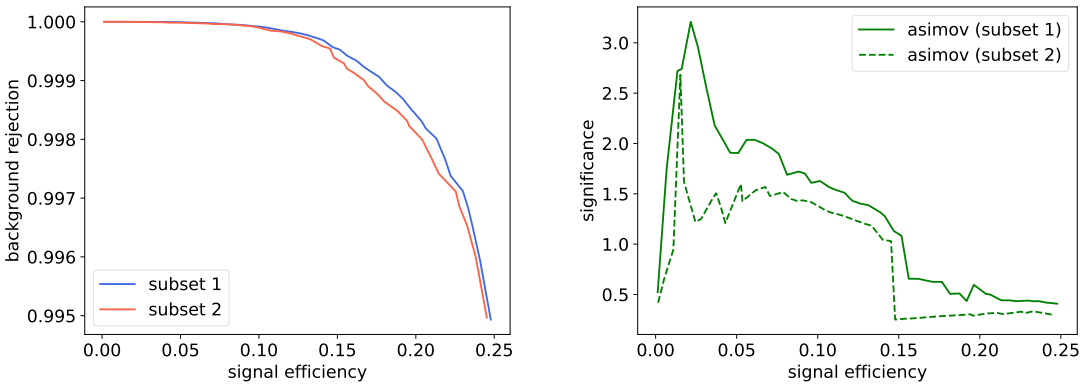

(a) ROC curve.

(b) significance scan.

Figure 6.12: ROC curve and significance scan for the optimization on the signal point with $m_{Z'} = 1000\,\text{GeV}$ and $m_s = 260\,\text{GeV}$. The optimization was performed using the large-R jet collection.

large-R jet or on τ_{21}. This cross-check confirms the signal region found in sec. 6.3.2 for the merged scenario.

In addition, an optimization with ahoi was performed using TAR jets with $R = 1.0$. The set of selections that were scanned was the same as in the optimization above, but with every large-R jet related variable replaced with the corresponding TAR jet variable. The results of this optimization showed that if using TAR jets the best possible expected significance is much lower than if defining the signal region with large-R jets. This reassures the choice of the jet collection made in this analysis. However, it does not give any insight into why TAR jets seem to perform so much worse than large-R jets. Since TAR jets were designed specifically to outperform standard jets in terms of identifying hadronic W-decays, this result is most counterintuitive and should be investigated further in future studies.

6.4 Statistical analysis

The general strategy of many searches for new physics is to prepare for two scenarios: If there is an excess visible in the data, the question is how significant that excess is. This gets determined by calculating the p-value, which is the probability of finding data that is more or equally inconsistent with the background-only hypothesis than the measured data. The larger the discrepancy of the observed data with the background-only hypothesis is, the smaller is p. An equivalent measure for p is the significance Z, defined as

$$Z = \Phi^{-1}(1 - p) \tag{6.4}$$

where Φ is the cumulative function of a Gaussian distribution [82]. Larger values of Z correspond to a larger inconsistency of the observed data with the hypothesis that only background processes are present.

The other scenario, the exclusion scenario, is that no excess is visible in the data. In this case the hypothesis test is performed in the other direction: How likely is it to find the observed data under the assumption that both signal and background are present? This has to be computed for every signal hypothesis (in the case of this analysis this means every signal point on the $m_{Z'}$-m_s-plane).

As a test statistic, the log profile likelihood ratio $q_{\mu_{\text{sig}}}$ [82, 83] is used. From this, the

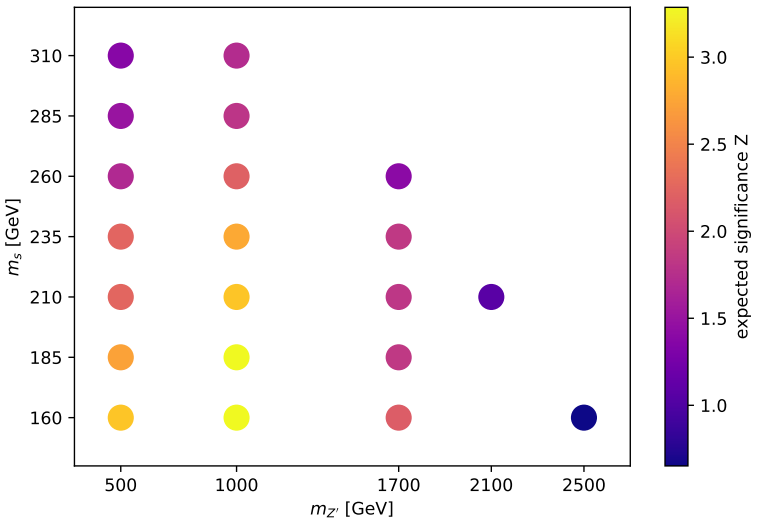

Figure 6.13: Expected significance for the different signal hypotheses.

CLs value is obtained. It is defined as

$$\mathrm{CLs} = \frac{p_{b+s}}{1 - p_b} \tag{6.5}$$

where p_{b+s} and p_b are the p-values of the signal+background and the background-only hypothesis, respectively. In the case where the distributions look very different under the signal+background hypothesis and the background-only hypothesis, CLs $\approx p_{b+s}$, so the intuition of a CLs value is very much the same as that of a p-value. If however both hypotheses result in distributions that are similar to each other, the CLs value gets larger, behaving like a more conservative "effective p-value". Thus the CLs method can be used to avoid false exclusions in case of low sensitivity. To exclude a given hypothesis, a value α must be set under which the CLs value must drop to be considered excluded. In the case of this analysis, $\alpha = 0.05$, meaning that signal hypotheses for which CLs < 0.05 are rejected. To put it differently, signal points get excluded at 95 % confidence level. The result can be visualized in a grid of all signal hypotheses. By interpolating between the CLs values of each signal point, a line where CLs $= 0.05$ can be drawn into the grid. This line is called *exclusion limit*. All signal points on one side of that line are then excluded with a confidence level of at least 95 %.

All calculations and visualizations related to the exclusion limit were performed with HistFitter [83]. Because in this analysis only MC generated data and no recorded data is used, all significances, CLs values and exclusion limits present expected, not observed, values.

6.4.1 Expected significance and limits

Fig. 6.13 shows the expected significances for all signal points. Almost all points reach a significance of $Z > 1.64$ which corresponds to $p < 0.05$ [82]. Surprisingly, Z is also extremely high for signal points that are expected to show a rather resolved event topology, namely the ones with $m_{Z'} \leq 1000\,\mathrm{GeV}$ and $m_s \leq 210\,\mathrm{GeV}$.

The expected exclusion limit is shown in fig. 6.14. It encloses most signal points, as it could already be expected given the good sensitivity seen in fig. 6.13. The color map shows

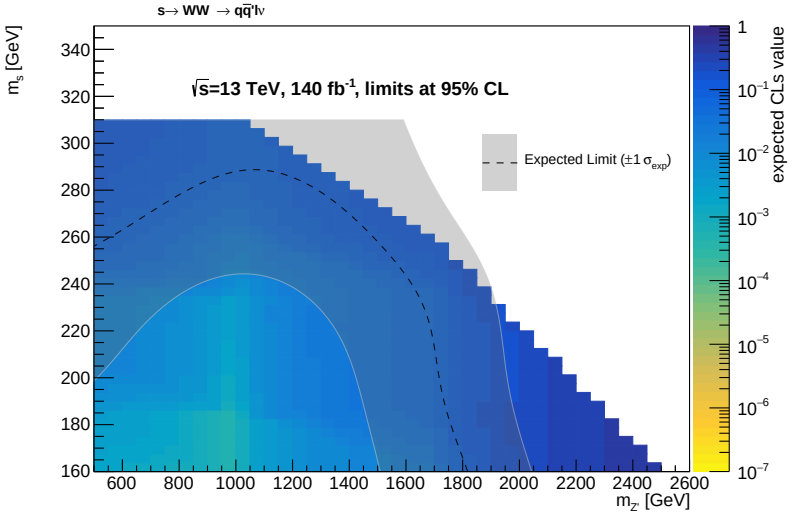

Figure 6.14: Exclusion plot using the signal region optimized for the merged scenario.

name	SR_dR0	SR_dR1
additional requirement on signal region	$\Delta R < 0.5$	$\Delta R \geq 0.5$

Table 6.3: Signal region binned in ΔR

the interpolated expected CLs values. Green and yellow regions correspond to very small CLs values, reflecting good sensitivity. The gray band indicates the uncertainty on the expected limit. It can be seen that it is cut off and continues along the upper edge of the signal grid. Because of the lack of signal points, no further interpolation is possible there. This suggests that the signal grid is too small and should be extended for future studies.

The next section shows how the expected exclusion limit can be improved and combines the results of this analysis with the results found in ref. [75] for the resolved scenario.

6.4.2 Sensitivity gain by introducing a multi-bin fit

As seen in the previous chapter, the signal region defined in sec. 6.3.2, optimized for the merged scenario, serves more or less all signal points and leads to an exclusion limit that encloses large parts of the parameter space. However, the exclusion limit can be improved by acknowledging that the signal region is still a compromise between multiple selection criteria that would fit better for some points on the signal grid. It is thus beneficial to split the signal region up in several subregions (*bins*) where each bin might increase the expected significance for different regions of the parameter space. If the subregions share no events, the significances that each bin yields can be combined, leading to an increased overall sensitivity.

The distribution of $\Delta R(\ell, j)$ (fig. 6.10b) for example looks quite different for signal samples with different $m_{Z'}$ or m_s, so it might be beneficial to introduce a binning in ΔR. The original signal region was split into two bins as listed in tab. 6.3. The resulting exclusion limits are shown in fig. 6.15a. There is a clear improvement in the expected limit, especially for signal points with larger $m_{Z'}$.

Next, a binning in the missing transverse energy significance $\mathcal{S}$ was introduced. Again,

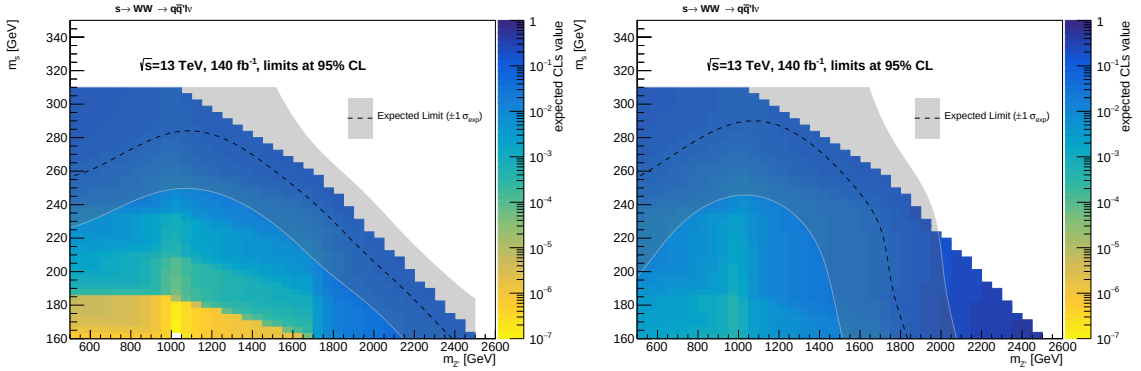

(a) With binning in ΔR.

(b) With binning in $\mathcal{S}$.

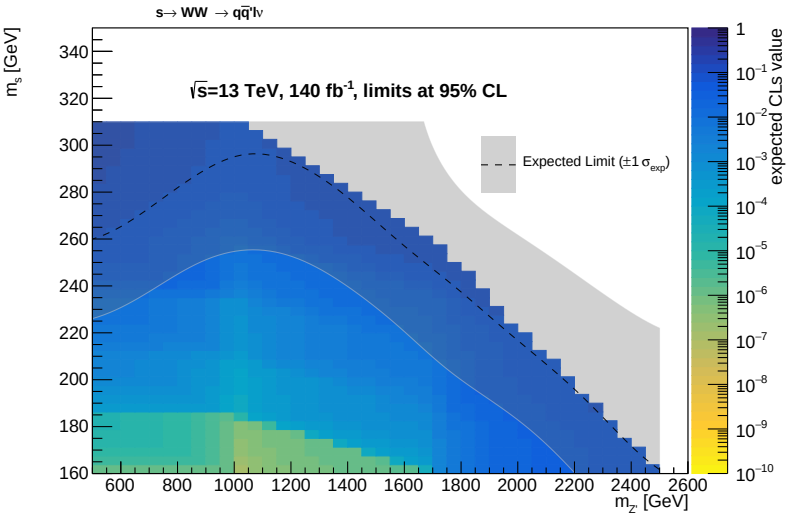

(c) With binning in both ΔR and $\mathcal{S}$. Note that, for comparability with fig. 6.17, the range of the Z-axis is much larger than in the two plots above, so the color-coding is not the same.

Figure 6.15: Expected exclusion limits using the signal region optimized for the merged scenario, but split into multiple regions using ΔR and $\mathcal{S}$.

the region was split into two disjoint subregions (see tab. 6.4). This binning does not improve the exclusion limit as much as the binning in ΔR did, but it does push the limit a little into regions of higher m_s (see fig. 6.15b).

The next step is to combine the two splittings to achieve an even better sensitivity. Ensuring orthogonality between the bins requires to define four separate regions. The final selection criteria for the merged region, together with the choice of bins, is listed in tab. 6.5. The exclusion limit that results from using these four signal regions can be seen in fig. 6.15c. It clearly combines the features of the exclusion limits obtained from binning in ΔR and $\mathcal{S}$ only, respectively. The limit excludes almost all points in the signal grid. Again, the uncertainty band hits the edges of the signal grid, showing that it is absolutely necessary to extend the signal grid to higher values of $m_{Z'}$ and m_s to continue with this analysis.

6.4.3 Combination of the merged and resolved regions

The signal regions presented here are however still optimized for the merged scenario only. The resolved category has been studied in ref. [75]. The optimal selection criteria for the

name	SR_S0	SR_S1
additional requirement on signal region	$\mathcal{S} \leq 22.5$	$\mathcal{S} > 22.5$

Table 6.4: Signal region binned in $\mathcal{S}$.

variable	**requirement**			
N_j	> 0			
$N_{b\text{-jets}}$	$= 0$			
$E_{\mathrm{T}}^{\mathrm{miss}}$	$> 300\,\mathrm{GeV}$			
m_{T}	$> 150\,\mathrm{GeV}$			
$m_{\text{large-}R\text{ jet}}$	$> 60\,\mathrm{GeV}$ and $< 100\,\mathrm{GeV}$			
$D_2^{\beta=1}$	< 1.4			
$\Delta R(\ell, j)$	< 0.5	< 0.5	≥ 0.5 and < 1.6	≥ 0.5 and < 1.6
$\mathcal{S}$	> 15 and ≤ 22.5	> 22.5	> 15 and ≤ 22.5	> 22.5

Table 6.5: Final signal regions for the merged scenario with binning in ΔR and $\mathcal{S}$.

resolved scenario are listed in tab. 6.6. Due to the lack of a large-R jet that reconstructs the hadronically decaying W-boson in the resolved region, a different approach to reconstruct the W is used here: The two anti-k_t jets with $R = 0.4$—out of the hardest three jets—whose combined invariant mass is closest to the mass of the W are combined and treated as the W-candidate. To further increase the sensitivity, the resolved region is split into five equally spaced bins in ΔR between the W-candidate and the lepton [75].

However, the merged and resolved signal selections overlap—in order to make the two regions orthogonal, the logical negation of the selection criteria for the merged region is added as an additional requirement. Fig. 6.16a shows the exclusion limit and expected CLs values when using the definition of the resolved region given in tab. 6.6 together with the binning in ΔR. In comparison, fig. 6.16b shows the same, but with the requirement that the resolved region shares no events with the merged region. It can be seen that this additional requirement decreases the sensitivity of the resolved region only slightly.

Combining the signal region optimized for the merged scenario in this analysis with the signal region optimized for the resolved region should yield an even better overall sensitivity.

variable	**requirement**
$E_{\mathrm{T}}^{\mathrm{miss}}$	$\geq 150\,\mathrm{GeV}$
number of b-jets	$= 0$
number of anti-k_t jets with $R = 0.4$	≥ 2
$m(W\text{-candidate})$	$> 60\,\mathrm{GeV}$ and $< 100\,\mathrm{GeV}$
m_{T}	$\geq 200\,\mathrm{GeV}$
$p_{\mathrm{T}}(W\text{-candidate})$	$\geq 100\,\mathrm{GeV}$
$\mathcal{S}$	≥ 13
$\Delta R(\ell, W\text{-candidate})$	≤ 1

Table 6.6: Selection criteria optimized for the resolved region [75].

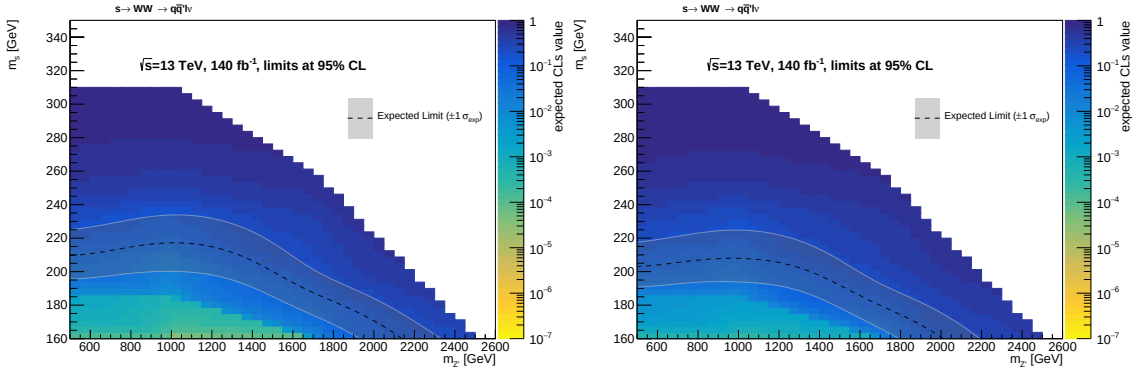

(a) Exclusion limit with original resolved region.

(b) Exclusion limit for resolved region with the additional requirement on orthogonality.

Figure 6.16: Exclusion limits for the resolved region without and with the additional requirement that the selection must be orthogonal to the merged region.

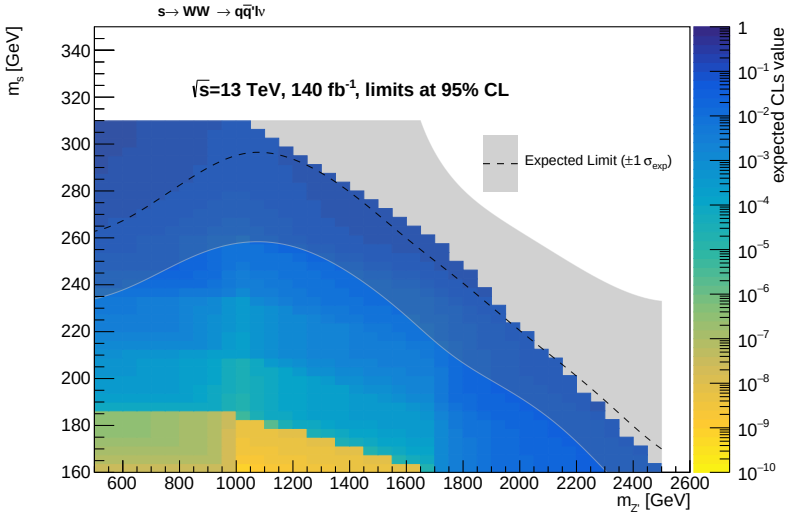

Figure 6.17: Final expected exclusion limit and CLs values for the combined signal regions.

The expected exclusion contour and CLs values are shown in fig. 6.17. When comparing the expected limit with the one in fig. 6.15c, it can be seen that including the resolved region changes almost nothing in the shape of the expected limit. This is not surprising, as the expected limit moves already at the very border of the signal grid. The expected CLs values however do improve, which can be seen in the brighter region of the color map.

This analysis shows that having a dedicated signal region for the merged scenario is essential when studying this signal model. The sensitivity gained by defining a merged region is high over almost the entire signal grid. The merged and resolved region work well together and improve the sensitivity further when combined.

7 Conclusion and outlook

MC simulated data of pp-collisions at a center of mass energy of $\sqrt{s} = 13\,\text{TeV}$ were used for a search for dark matter. The model considered here predicts dark matter particles to be produced in association with a dark Higgs boson s. The analysis presented concentrates on the case of a strongly boosted dark Higgs and its subsequent decay into two W-bosons which then further decay semileptonically, resulting in a signature with one charged lepton, one large-R jet and high missing transverse energy.

The mass distributions of TAR jets with radius parameters $R = 0.6$, $R = 0.8$, $R = 1.0$ and standard anti-k_t jets with $R = 1.0$ (large-R jets) were compared with respect to their ability to reconstruct a W-boson decaying into one boosted jet. Large-R jets were found to outperform TAR jets. A satisfying explanation why the performance of the TAR jets is apparently worse than the large-R jets could not be given. Since TAR jets were previously shown to provide an improved performance of identifying boosted hadronic W-decays [64], this matter should be subject to future studies.

An optimization of the signal region for the merged scenario was presented. The defined selection criteria for the signal region were then cross-checked and verified by an extensive automated scan over other possible selection criteria. This cross-check was also able to serve as an additional justification to use large-R jets and not TAR jets in this analysis.

Finally, a statistical analysis of the MC data was performed. It was shown that the selection criteria that were found to be optimal for the merged region yield a high expected significance for almost all generated signal points. The expected CLs values in the case that the recorded data shows no excess over the expected background were calculated. The resulting exclusion limit at 95 % confidence level can be further improved by splitting the signal region up in several subregions, divided by additional requirements on the distance ΔR between the lepton and the large-R jet, taking advantage of the differences in the shape of ΔR for different signal points and on the missing transverse energy significance $\mathcal{S}$. The expected exclusion limit encloses almost the entire generated signal grid, reaching up to Z' masses of $m_{Z'} \approx 2500\,\text{GeV}$ and dark Higgs masses of $m_s \approx 300\,\text{GeV}$. This result shows that, for further studies, the signal grid has to be extended to larger values of $m_{Z'}$ and m_s since the sensitivity achieved in this analysis is limited by the size of the generated grid. When extending the signal grid to higher values of m_s, it should be noted that one motivation for the dark matter model considered here is its ability to reproduce the dark matter relic abundance if the dark Higgs s is too light to decay into particles of the dark sector. With the current choice of $m_\chi = 200\,\text{GeV}$, the mass of the dark Higgs should satisfy $m_s < 400\,\text{GeV}$ to not violate this constraint.

To continue this analysis it will be necessary to check if the choice of the signal regions is still valid with the extended grid and, if needed, to adjust them accordingly. Then, the definition of control and validation regions will be needed. Control regions are regions in phase space where the amount of expected signal events is negligible. They are used to compare the MC data to recorded data and derive scale factors that align the MC distributions to the recorded data in the control regions. These scale factors can then be extrapolated into the signal region. To check that the extrapolation works correctly, validation regions are introduced. In these regions, the signal contamination is still negligible. The validation regions should lie in between the control and signal regions. Finally, after

studying and taking into account all systematic uncertainties, the MC data in the signal region may be compared to recorded data, resulting in either a discovery or an exclusion.

List of Figures

List of Tables

Bibliography

[1] S. L. Glashow, J. Iliopoulos, and L. Maiani. "Weak Interactions with Lepton-Hadron Symmetry". *Phys. Rev.* D2 (1970), pp. 1285–1292.

[2] F. Englert and R. Brout. "Broken Symmetry and the Mass of Gauge Vector Mesons". *Phys. Rev. Lett.* 13 (1964), pp. 321–323.

[3] P. W. Higgs. "Broken Symmetries and the Masses of Gauge Bosons". *Phys. Rev. Lett.* 13 (1964), pp. 508–509.

[4] ATLAS Collaboration. "Observation of a new particle in the search for the Standard Model Higgs boson with the ATLAS detector at the LHC". *Phys. Lett.* B716 (2012), pp. 1–29. arXiv: 1207.7214 [hep-ex].

[5] CMS Collaboration. "Observation of a New Boson at a Mass of 125 GeV with the CMS Experiment at the LHC". *Phys. Lett.* B716 (2012), pp. 30–61. arXiv: 1207.7235 [hep-ex].

[6] S. T. Thornton and J. B. Marion. *Classical Dynamics of Particles and Systems*. Fifth edition. Thomson Brooks/Cole, 2004, pp. 260–261. ISBN: 0-534-40896-6.

[7] D. Morin. *Introduction to Classical Mechanics: With Problems and Solutions*. Cambridge University Press, 2008. ISBN: 9781139468374. URL: https://books.google.de/books?id=Ni6CD7K2X4MC.

[8] D. J. Griffiths. *Introduction to elementary particles; 2nd rev. version*. Physics textbook. New York, NY: Wiley, 2008. URL: https://cds.cern.ch/record/111880.

[9] M. Thomson. *Modern particle physics*. New York: Cambridge University Press, 2013. ISBN: 9781107034266.

[10] A. Pich. "The Standard model of electroweak interactions". 2008, pp. 1–49. arXiv: 0705.4264 [hep-ph]. URL: http://doc.cern.ch/yellowrep/2007/2007-005/cern-2007-005.pdf.

[11] S. Schael et al. "Electroweak Measurements in Electron-Positron Collisions at W-Boson-Pair Energies at LEP". *Phys. Rept.* 532 (2013), pp. 119–244. arXiv: 1302.3415 [hep-ex].

[12] S. Schael et al. "Precision electroweak measurements on the Z resonance". *Phys. Rept.* 427 (2006), pp. 257–454. arXiv: hep-ex/0509008 [hep-ex].

[13] M. E. Peskin and D. V. Schroeder. *An Introduction to quantum field theory*. Reading, USA: Addison-Wesley, 1995, pp. 689–692. ISBN: 9780201503975, 0201503972.

[14] Y. Fukuda et al. "Evidence for oscillation of atmospheric neutrinos". *Phys. Rev. Lett.* 81 (1998), pp. 1562–1567. arXiv: hep-ex/9807003 [hep-ex].

[15] M. Kaku. *Quantum Field Theory: A Modern Introduction*. Oxford University Press, 1993. ISBN: 9780195091588.

[16] C. Burgess and G. Moore. *The Standard Model: A Primer*. Cambridge University Press, 2006. ISBN: 9781139460460. URL: https://books.google.de/books?id=PLYECqs2geEC.

[17] O. Lahav and A. R. Liddle. "The Cosmological Parameters 2014" (2014). arXiv: 1401.1389 [astro-ph.CO].

[18] N. Jarosik et al. "Seven-Year Wilkinson Microwave Anisotropy Probe (WMAP) Observations: Sky Maps, Systematic Errors, and Basic Results". *Astrophys. J. Suppl.* 192 (2011), p. 14. arXiv: 1001.4744 [astro-ph.CO].

[19] A. Bosma. "The distribution and kinematics of neutral hydrogen in spiral galaxies of various morphological types". PhD thesis. 1978.

[20] E. Corbelli and P. Salucci. "The Extended Rotation Curve and the Dark Matter Halo of M33". *Mon. Not. Roy. Astron. Soc.* 311 (2000), pp. 441–447. arXiv: astro-ph/9909252 [astro-ph].

[21] T. A. Porter, R. P. Johnson, and P. W. Graham. "Dark Matter Searches with Astroparticle Data". *Ann. Rev. Astron. Astrophys.* 49 (2011), pp. 155–194. arXiv: 1104.2836 [astro-ph.HE].

[22] N. Aghanim et al. "Planck 2018 results. VI. Cosmological parameters" (2018). arXiv: 1807.06209 [astro-ph.CO].

[23] C. Boehm and R. Schaeffer. "Constraints on dark matter interactions from structure formation: Damping lengths". *Astron. Astrophys.* 438 (2005), pp. 419–442. arXiv: astro-ph/0410591 [astro-ph].

[24] G. Bertone and D. Merritt. "Dark matter dynamics and indirect detection". *Mod. Phys. Lett.* A20 (2005), p. 1021. arXiv: astro-ph/0504422 [astro-ph].

[25] J. M. Lorenz. "Supersymmetry and the collider Dark Matter picture". *Mod. Phys. Lett.* A34.30 (2019), p. 1930005. arXiv: 1908.09672 [hep-ex].

[26] M. Duerr et al. "Hunting the dark Higgs". *JHEP* 04 (2017), p. 143. arXiv: 1701.08780 [hep-ph].

[27] M. Duerr et al. "How to save the WIMP: global analysis of a dark matter model with two s-channel mediators". *JHEP* 09 (2016), p. 042. arXiv: 1606.07609 [hep-ph].

[28] ATLAS Collaboration. "Search for Dark Matter Produced in Association with a Higgs Boson decaying to $b\bar{b}$ at $\sqrt{s} = 13\,\text{TeV}$ with the ATLAS Detector using $79.8\,\text{fb}^{-1}$ of proton-proton collision data". ATLAS-CONF-2018-039 (2018). Conference Note. URL: https://cds.cern.ch/record/2632344.

[29] ATLAS Collaboration. "Search for Dark Matter Produced in Association with a Hypothetical Scalar Boson Decaying to W^+W^- in the $q\bar{q}'q\bar{q}'$ final state at $\sqrt{s} = 13\,\text{TeV}$ using $139\,\text{fb}^{-1}$ of pp collisions recorded with the ATLAS Detector". ANA-EXOT-2018-40-INT1 (2020). Internal Note.

[30] D. Abercrombie et al. "Dark Matter Benchmark Models for Early LHC Run-2 Searches: Report of the ATLAS/CMS Dark Matter Forum". *Phys. Dark Univ.* 26 (2019). Ed. by A. Boveia et al., p. 100371. arXiv: 1507.00966 [hep-ex].

[31] J. Haffner. *The CERN accelerator complex.* URL: http://cds.cern.ch/images/OPEN-PHO-ACCEL-2013-056-1 (visited on 03/22/2020).

[32] L. Evans and P. Bryant. "LHC Machine". *JINST* 3 (2008), S08001.

[33] *Detector and Technology.* URL: http://atlas.cern/discover/detector (visited on 03/22/2020).

[34] *LHC report: Full house for the LHC.* URL: https://home.cern/news/news/accelerators/lhc-report-full-house-lhc (visited on 04/03/2020).

[35] ALICE Collaboration. "The ALICE experiment at the CERN LHC". *JINST* 3 (2008), S08002.

[36] LHCb Collaboration. "The LHCb Detector at the LHC". *JINST* 3 (2008), S08005.

[37] ATLAS Collaboration. "The ATLAS Experiment at the CERN Large Hadron Collider". *Journal of Instrumentation* 3.08 (2008), S08003–S08003. URL: https://doi.org/10.1088%2F1748-0221%2F3%2F08%2Fs08003.

[38] CMS Collaboration. "The CMS Experiment at the CERN LHC". *JINST* 3 (2008), S08004.

[39] A. La Rosa. "The ATLAS Insertable B-Layer: from construction to operation". *Proceedings, 8th International Workshop on Semiconductor Pixel Detectors for Particles and Imaging (PIXEL 2016): Sestri Levante, Italy, September 5-9, 2016*. Vol. 11. 12. 2016, p. C12036. arXiv: 1610.01994 [physics.ins-det].

[40] ATLAS Collaboration. "ATLAS pixel detector electronics and sensors". *Journal of Instrumentation* 3.07 (2008), P07007–P07007. URL: https://doi.org/10.1088%2F1748-0221%2F3%2F07%2Fp07007.

[41] A. Ahmad et al. "The Silicon microstrip sensors of the ATLAS semiconductor tracker". *Nucl. Instrum. Meth.* A578 (2007), pp. 98–118.

[42] ATLAS TRT Collaboration. "The ATLAS Transition Radiation Tracker (TRT) proportional drift tube: Design and performance". *JINST* 3 (2008), P02013.

[43] N. Kerschen and the ATLAS test beam group. "Performance of the ATLAS liquid argon barrel calorimeter in the 2004 combined test beam". *Journal of Physics: Conference Series* 160 (2009), p. 012049. URL: https://doi.org/10.1088%2F1742-6596%2F160%2F1%2F012049.

[44] P. Francavilla and the ATLAS Collaboration. "The ATLAS Tile Hadronic Calorimeter performance at the LHC". *Journal of Physics: Conference Series* 404 (2012), p. 012007. URL: https://doi.org/10.1088%2F1742-6596%2F404%2F1%2F012007.

[45] ATLAS Level-1 Trigger Group. *ATLAS level-1 trigger: Technical Design Report*. Technical Design Report ATLAS. Geneva: CERN, 1998. URL: http://cds.cern.ch/record/381429.

[46] ATLAS Collaboration. "The Run-2 ATLAS Trigger System". ATL-DAQ-PROC-2016-003 (2016). URL: https://cds.cern.ch/record/2133909.

[47] ATLAS Collaboration. "Fast TracKer (FTK) Technical Design Report". CERN-LHCC-2013-007. ATLAS-TDR-021 (2013). ATLAS Fast Tracker Technical Design Report. URL: http://cds.cern.ch/record/1552953.

[48] ATLAS Collaboration. *ATLAS high-level trigger, data-acquisition and controls: Technical Design Report*. Technical Design Report ATLAS. Geneva: CERN, 2003. URL: http://cds.cern.ch/record/616089.

[49] ATLAS Collaboration. "The Run-2 ATLAS Trigger System". *Journal of Physics: Conference Series* 762 (2016), p. 012003. URL: https://doi.org/10.1088%2F1742-6596%2F762%2F1%2F012003.

[50] A. Buckley et al. "General-purpose event generators for LHC physics". *Phys. Rept.* 504 (2011), pp. 145–233. arXiv: 1101.2599 [hep-ph].

[51] W. Herr and B Muratori. "Concept of luminosity" (2006). URL: https://cds.cern.ch/record/941318.

[52] ATLAS Collaboration. "Luminosity determination in pp collisions at $\sqrt{s} = 13$ TeV using the ATLAS detector at the LHC". ATLAS-CONF-2019-021 (2019). URL: http://cds.cern.ch/record/2677054.

[53] E. Bothmann et al. "Event Generation with Sherpa 2.2". *SciPost Phys.* 7.3 (2019), p. 034. arXiv: 1905.09127 [hep-ph].

[54] S. Alioli et al. "A general framework for implementing NLO calculations in shower Monte Carlo programs: the POWHEG BOX". *JHEP* 06 (2010), p. 043. arXiv: 1002.2581 [hep-ph].

[55] T. Sjöstrand et al. "An Introduction to PYTHIA 8.2". *Comput. Phys. Commun.* 191 (2015), pp. 159–177. arXiv: 1410.3012 [hep-ph].

[56] J. Alwall et al. "The automated computation of tree-level and next-to-leading order differential cross sections, and their matching to parton shower simulations". *JHEP* 07 (2014), p. 079. arXiv: 1405.0301 [hep-ph].

[57] S. Agostinelli et al. "GEANT4: A Simulation toolkit". *Nucl. Instrum. Meth.* A506 (2003), pp. 250–303.

[58] ATLAS Collaboration. "Electron reconstruction and identification in the ATLAS experiment using the 2015 and 2016 LHC proton-proton collision data at $\sqrt{s} = 13$ TeV". *Eur. Phys. J.* C79.8 (2019), p. 639. arXiv: 1902.04655 [physics.ins-det].

[59] ATLAS Collaboration. "Electron and photon reconstruction and performance in ATLAS using a dynamical, topological cell clustering-based approach". ATL-PHYS-PUB-2017-022 (2017). URL: https://cds.cern.ch/record/2298955.

[60] ATLAS Collaboration. "Muon reconstruction performance of the ATLAS detector in proton–proton collision data at $\sqrt{s}$ =13 TeV". *Eur. Phys. J.* C76.5 (2016), p. 292. arXiv: 1603.05598 [hep-ex].

[61] ATLAS collaboration. "Measurement of the tau lepton reconstruction and identification performance in the ATLAS experiment using pp collisions at $\sqrt{s} = 13\,\text{TeV}$" (2017).

[62] M. Cacciari, G. P. Salam, and G. Soyez. "The anti-k_t jet clustering algorithm". *JHEP* 04 (2008), p. 063. arXiv: 0802.1189 [hep-ph].

[63] ATLAS Collaboration. "Tagging and suppression of pileup jets with the ATLAS detector". ATLAS-CONF-2014-018 (2014). URL: https://cds.cern.ch/record/1700870.

[64] ATLAS Collaboration. "Track assisted techniques for jet substructure". ATL-PHYS-PUB-2018-012 (2018). URL: https://cds.cern.ch/record/2630864.

[65] M. Cacciari, G. P. Salam, and G. Soyez. "FastJet User Manual". *Eur. Phys. J.* C72 (2012), p. 1896. arXiv: 1111.6097 [hep-ph].

[66] ATLAS Collaboration. "Expected performance of the ATLAS b-tagging algorithms in Run-2". ATL-PHYS-PUB-2015-022 (2015). URL: https://cds.cern.ch/record/2037697.

[67] ATLAS Collaboration. "Optimisation of the ATLAS b-tagging performance for the 2016 LHC Run". ATL-PHYS-PUB-2016-012 (2016). URL: https://cds.cern.ch/record/2160731.

[68] A. D. Martin et al. "Parton distributions for the LHC". *Eur. Phys. J.* C63 (2009), pp. 189–285. arXiv: 0901.0002 [hep-ph].

[69] ATLAS Collaboration. "Performance of missing transverse momentum reconstruction with the ATLAS detector using proton-proton collisions at $\sqrt{s} = 13\,\text{TeV}$". *Eur. Phys. J.* C78.11 (2018), p. 903. arXiv: 1802.08168 [hep-ex].

[70] ATLAS Collaboration. "Object-based missing transverse momentum significance in the ATLAS detector". ATLAS-CONF-2018-038 (2018). URL: https://cds.cern.ch/record/2630948.

[71] ATLAS Collaboration. "Data-Quality Requirements and Event Cleaning for Jets and Missing Transverse Energy Reconstruction with the ATLAS Detector in Proton-Proton Collisions at a Center-of-Mass Energy of *sqrts* = 7 TeV". ATLAS-CONF-2010-038 (2010). URL: http://cds.cern.ch/record/1277678.

[72] ATLAS Collaboration. "Search for Dark Matter Produced in Association with a Hypothetical Scalar Boson Decaying to W^+W^- in the $q\overline{q}'\ell\nu$ final state at $\sqrt{s} = 13\,\text{TeV}$ using $139\,\text{fb}^{-1}$ of pp collisions recorded with the ATLAS Detector" (to be published). Internal Support Note.

[73] E. Boos and L. Dudko. "The Single Top Quark Physics". *Int. J. Mod. Phys.* A27 (2012), p. 1230026. arXiv: 1211.7146 [hep-ph].

[74] W. Wagner. "Top quark physics in hadron collisions". *Rept. Prog. Phys.* 68 (2005), pp. 2409–2494. arXiv: hep-ph/0507207 [hep-ph].

[75] R. Weber. "Search for Dark Matter in Association of a Dark Higgs Boson". MA thesis. Ludwig-Maximilians-Universität München, 2020.

[76] R. Brun and F. Rademakers. "ROOT: An object oriented data analysis framework". *Nucl. Instrum. Meth.* A389 (1997), pp. 81–86.

[77] ATLAS Collaboration. "Measurement of the W-boson mass in pp collisions at $\sqrt{s} = 7\,\text{TeV}$ with the ATLAS detector". *Eur. Phys. J.* C78.2 (2018). [Erratum: Eur. Phys. J.C78,no.11,898(2018)], p. 110. arXiv: 1701.07240 [hep-ex].

[78] ATLAS Collaboration. "Search for chargino and neutralino production in final states with a Higgs boson and missing transverse momentum at $\sqrt{s} = 13$ TeV with the ATLAS detector". *Phys. Rev.* D100.1 (2019), p. 012006. arXiv: 1812.09432 [hep-ex].

[79] A. J. Larkoski, G. P. Salam, and J. Thaler. "Energy Correlation Functions for Jet Substructure". *JHEP* 06 (2013), p. 108. arXiv: 1305.0007 [hep-ph].

[80] ATLAS Collaboration. "Identification of boosted, hadronically decaying W bosons and comparisons with ATLAS data taken at $\sqrt{s} = 8$ TeV". *Eur. Phys. J.* C76.3 (2016), p. 154. arXiv: 1510.05821 [hep-ex].

[81] A. J. Larkoski, I. Moult, and D. Neill. "Analytic Boosted Boson Discrimination". *JHEP* 05 (2016), p. 117. arXiv: 1507.03018 [hep-ph].

[82] G. Cowan et al. "Asymptotic formulae for likelihood-based tests of new physics". *Eur. Phys. J.* C71 (2011). [Erratum: Eur. Phys. J.C73,2501(2013)], p. 1554. arXiv: 1007.1727 [physics.data-an].

[83] M. Baak et al. "HistFitter software framework for statistical data analysis". *Eur. Phys. J.* C75 (2015), p. 153. arXiv: 1410.1280 [hep-ex].

Danksagung

Ich möchte mich ganz herzlich bei Prof. Dorothee Schaile bedanken, dass sie mir die Möglichkeit gegeben hat, an ihrem Lehrstuhl diese Masterarbeit zu schreiben, sowie für das Korrekturlesen der Arbeit.

Ganz besonderer Dank gilt Dr. Jeanette Lorenz für ihre hervorragende Betreuung, ihre Unterstützung und ihre immer konstruktive Kritik, sowie für das Korrekturlesen der Arbeit.

Außerdem möchte ich mich bei allen Mitgliedern am Lehrstuhl für die angenehme und hilfsbereite Atmosphäre bedanken – insbesondere bei Andrea Matić und Eric Schanet, die mir unzählige Male bei technischen oder physikalischen Fragen weitergeholfen haben. Danke auch an Dr. Nikolai Hartmann für die von ihm entwickelte und frei zur Verfügung gestellte Software MPF und ahoi.

I would also like to thank all members of the MonoS(WW)-hadronic and MonoS(VV)-leptonic analysis team for their constructive feedback and for providing many many lines of code that I used for this thesis.

Ich möchte mich auch bei meinen Eltern bedanken, die mich während meinem gesamten Studium bedingungslos unterstützt haben.

Vielen Dank auch an meine Eltern und an Jannis für ihre sprachlichen Verbesserungsvorschläge in dieser Arbeit.

Zu guter Letzt möchte ich mich bei allen meinen Freunden bedanken, dafür dass sie immer für mich da sind. Besonders bei Michi, Philipp und Manu, ohne die das Physikstudium für mich nicht halb so viel Spaß gemacht hätte. Und natürlich bei allen meinen Mitbewohnerinnen und Mitbewohnern, Johanna, Elli, Luca und Inés, die mich in der zum Teil stressigen Zeit während der Masterarbeit immer aufgebaut und motiviert haben – Danke!

Erklärung

Hiermit erkläre ich, die vorliegende Arbeit selbständig verfasst zu haben und keine anderen als die in der Arbeit angegebenen Quellen und Hilfsmittel benutzt zu haben.

David Koch
München, 22. April 2020